이학석사 학위논문

Unveiling the clearance mechanism of cellular lipid droplets by inducing autophagy with SB2301

자가포식작용을 유도하는 물질을 통한 새로운
지방방울 제거 메커니즘의 발굴

2021년 8월

서울대학교 대학원
화학부 화학생물학 전공
박 종 범

Unveiling the clearance mechanism of cellular lipid droplets by inducing autophagy with SB2301

지도 교수 박 승 범

이 논문을 이학석사 학위논문으로 제출함

2021년 6월

서울대학교 대학원

화학부 화학생물학 전공

박 종 범

박종범의 이학석사 학위논문을 인준함

2020년 6월

위 원 장 _____

부위원장 _____

위 원 _____

Abstract

Unveiling the clearance mechanism of cellular lipid droplets by inducing autophagy with SB2301

Park JongBeom

Chemical Biology major

Department of Chemistry

Seoul National University

Cells utilize stored lipids as an energy source in two ways: lipolysis and lipophagy. Lipophagy, a subset of selective autophagy, was first reported in 2009, and thereafter studies have been steadily reporting that lipophagy plays an important role in lipid metabolism. For instance, disturbances in lipophagy are highly correlated to various metabolic diseases such as non-alcoholic fatty liver disease (NAFLD). However, despite this significance, the detailed regulatory mechanisms remain poorly elucidated compared to other types of selective autophagy. In addition, the lack of suitable reference compounds for studying lipophagy is one of the limitations of this research field.

In this dissertation, I reported a novel lipophagy inducing small molecule, **SB2301**. This small molecule activates lipophagy in a different way from other autophagy inducers such as rapamycin. **SB2301** was discovered from pDOS library using an image-based high throughput screening system. Further mechanistic studies

revealed that **SB2301** alters the phospholipid composition on the lipid droplet membrane and makes it unstable. The destabilized lipid droplets spontaneously merge and become ubiquitinated for degradation. By inducing autophagy with **SB2301**, I unveiled that a ubiquitin-mediated lipophagy mechanism exists and that changing lipid droplet membrane composition can induce lipophagy. This drug discovery shows potential breakthroughs for studying lipophagy.

Keywords: lipophagy, bioactive small molecule, phospholipid composition, ubiquitin-mediated lipophagy

Student Number: 2019-26485

Table of Contents

List of Figures

List of Table

1. Introduction

Lipid droplets (LDs) are organelles that store various lipids, such as triacylglycerols (TAGs) and sterol esters (SEs) in cells.[1] LDs are very dynamic organelles, and their size and number are regulated by cellular metabolic conditions.[2,3] In the nutrient-rich state, cells convert excess acetyl-COA into malonyl-COA to synthesize free fatty acids.[4] They rapidly convert these free fatty acids into TAGs and store them in LDs to avoid lipotoxicity.[5,6] Through this process, the size and number of LDs increase. In contrast, cells utilize stored TAGs as an energy source upon starvation.[1,7] TAGs are converted to free fatty acids and transported into the mitochondria, where they undergo beta-oxidation.[3,8] By regulating the influx of substrates for this energy-yielding process, LDs play a crucial role in maintaining energy homeostasis and regulating lipid metabolism.[9]

Cells catabolize stored lipids via two intracellular mechanisms, lipolysis and lipophagy.[10] Lipolysis involves several cytoplasmic lipases that act on the LD surface to degrade stored TAGs.[11] Cells regulate lipolysis by controlling lipase activity largely through post-translational modifications such as phosphorylation.[12] Nutrient depletion and hormones are the major factors activating lipolysis, and the underlying regulatory mechanisms have been well-studied.[11,13] Compared to lipolysis, lipophagy is a more recently discovered mechanism. In 2009, a report elucidated that autophagy is involved in lipid metabolism.[14] This publication illustrated lipophagy as a type of selective autophagy that targets LDs and found that lipid accumulation occurred when autophagy was downregulated. Since then, lipophagy has been accepted as a major mechanism of removing intracellular LDs.[15-17] Unlike lipolysis, lipophagy involves two organelles

that degrade entire LDs: autophagosomes and lysosomes.[18,19] When cells are exposed to a nutrient-deficient environment, double-membrane structures called autophagosomes form near the LDs and subsequently engulf the neighboring LDs before fusing with lysosomes to form autolysosomes.[11,14] Lysosomal acid lipases (LALs) in the autolysosomes degrade TAGs, and the free fatty acids are released to the cytosol.[10,16]

Recent studies have reported the relationship between lipophagy and metabolic diseases, such as non-alcoholic fatty liver disease (NAFLD).[20] Autophagic activity is generally lower in obesity, type 2 diabetes, and NAFLD patients.[20,21] In addition, lipophagy dysregulation is a pathogenetic factor in the development of NAFLD.[21] Thus, upregulating lipophagy with caloric restriction mimetics (CRMs) is a major strategy to alleviate metabolic diseases.[22] However, despite the clinical importance of lipophagy, its mechanisms remain poorly elucidated compared to other types of selective autophagy.[10,23]

In this study, I discovered a novel lipophagy inducer called **SB2301** and its mode of action. Interestingly, **SB2301** activates lipophagy without affecting nutrient-sensing pathways. It alters the phospholipid composition on the LD membrane, rendering it unstable. Destabilized LDs spontaneously merge and are degraded by autophagic machinery. This LD clearance mechanism has not been previously reported and suggests a novel way to induce lipophagy.

2. Materials and methods

Antibodies and plasmids Anti-LC3B (ab51520), anti-PCYT2 (ab126142), anti-IDH1(ab81653), anti-p62 (ab91526), anti- TOMM40 (ab185543), anti-PLIN2 (ab108323) and anti-ubiquitin (ab7780) were purchased from Abcam. Anti-GAPDH (CST 2118), anti-Rab7 (CST 9367), anti-Bip (CST 3183) HRP-labeled anti-mouse IgG (CST 7076), and HRP-labeled anti-rabbit IgG secondary antibodies (CST 7074) were purchased from Cell Signaling Technology. Anti-WDR1 (sc-393159), anti- ACSL4 (sc-271800) were purchased from SantaCruz. mCherry-GFP-LC3 plasmid (pBabe vector) was given from Dr. Heesun Cheong, Division of Chemical Biology, Research Institute, National Cancer Center, Korea. mCherry-LC3 plasmid was purchased from Addgene (40827).

Imaging Instrument DeltaVision Elite imaging system from GE Healthcare was used for high-resolution imaging experiments. Objective lenses were equipped with Olympus IX-71 inverted microscope. sCMOS camera and InSightSSI fluorescence illumination module were equipped with the system. For live cell imaging, CO2 supporting chamber with an objective air heater was installed with the system. Images were analyzed with SoftWorks program supported by GE Healthcare.

Cell Culture HepG2 cells were cultured in Dulbecco modified eagle medium (DMEM) with 10% (v/v) fetal bovine serum (FBS), and 1% (v/v) antibiotic-antimycotic (AA) solution. HeLa cells were cultured in RPMI 1640 medium with 10% (v/v) FBS, and 1% AA solution. AML12 cells were cultured in DMEM/F12 (1:1) (Gibco, 11330-032), 1× insulin-transferrin-selenium-G Supplement (Gibco, 41400-045), dexametasone (final 40 ng/ml), 10% (v/v) FBS, and 1% (v/v) AA solution. Cells were maintained in 100-mm cell culture dish in an incubator at 37 ºC, in a humidified atmosphere with 5% CO2.

LD imaging with SF44 Live cells were treated with SF44 (10 μM) and Hoechst 33342 (2 μg/ml). Serum-free condition (as a positive control) was changed to complete media before treatment with SF44 and Hoechst. After 30 min of incubation, automatic fluorescence imaging was performed with InCell Analyzer 2000 [GE Healthcare] or DeltaVision Elite [GE Healthcare] without washing. Using InCell Analyzer 2000, images of four randomly selected spots per individual well in a 96-well plate were automatically captured. Images were taken in auto-focusing mode at a 20× magnification. Fluorescence imaging was performed using the following filter settings: excitation_emission, 430/24 nm_605/64 nm for LD; 350/50 nm_455/50 nm for nucleus in InCell Analyzer 2000 or 438/24 nm_559/38 nm for LD; 380/18 nm_435/48 nm for nucleus in DeltaVision Elite. Data were analyzed using InCell Developer

program, according to the manufacturer's protocol. The fluorescence intensity of LD was interpreted as a cellular organelle using a granularity module, and the area of individual cells was recognized by nuclei staining using collar segmentation.

Western Blotting Cells were lysed with radio-immunoprecipitation assay (RIPA) buffer (50 mM Tris, pH 7.8, 150 mM NaCl, 0.5% deoxycholate, 1% IGEPAL CA-630) and protease inhibitor cocktail (Roche). Proteins were obtained after centrifugation at 15000 rpm for 20 min, by transferring the supernatant. Protein concentration was quantified with BCA protein assay kit. Overall protein sampling procedures were done at 4 ºC. Prepared protein samples were analyzed with SDS-PAGE followed by western blot procedure. Proteins were transferred into PVDF membrane, and it was blocked with 2% BSA in TBST over 1 h on r. t. Primary antibodies were treated overnight at 4 ºC followed by washing with TBST. HRP-labeled anti-rabbit IgG or HRP-labeled anti-mouse IgG secondary antibody (1:5000) were treated at r.t. for 1 h. After washing with TBST, membrane was developed by Amersham ECL prime solution. Chemiluminescent signal was measured by ChemiDoc MP imaging system.

Transfection HeLa cells were seeded on Lab-Tek II Chambered Coverglass w/Cover #1.5 Borosilicate Sterile/8 Well (Nunc 155409),

24 h before transfection. mCherry-GFP-LC3 plasmid or mCherry-hLC3 plasmid was transfected to HeLa cells using Lipofectamine 2000 reagent (Invitrogen, 11668019). Transfection was proceeded according to manufacturer's protocol.

mCherry-GFP-LC3 puncta imaging Fluorescence images from HeLa cells transfected mCherry-GFP-LC3 were obtained with 60× scale, using mCherry/mCherry, GFP/GFP (Excitation/Emission) filter sets. mCherry (excitation: 575/25 nm, emission: 625/45 nm); and GFP (excitation: 475/28 nm, emission: 525/48 nm). Images were analyzed with SoftWorks deconvolution software.

mCherry-hLC3 and LD imaging DeltaVision Elite imaging system was used for the imaging of mCherry-hLC3 transfected HeLa cells. For live-cell imaging, the chamber was maintained at 37 ℃, 5% CO_2 condition. Before imaging, LDs were stained with SF44 (10 μM) for 30 min. The image was obtained with 100× scale, using mCherry/mCherry, CFP/YFP (Excitation/Emission) filter sets. mCherry (excitation: 575/25 nm, emission: 625/45 nm); and CFP/YFP (excitation: 438/24 nm, emission: 559/38 nm). Images were analyzed with SoftWorks deconvolution software.

Lysosome and LD imaging Before fluorescence imaging, lysosomes were stained with Lysotracker DeepRed (50 nM, Thermo

Scientific, L7528) for 1.5 h. LDs were stained with SF44 (10 μM) and nuclei were stained with Hoechst 33342 (2 μg/ml) for 30 min. Images were obtained at a magnification of 100× using Cy5/Cy5, (excitation_emission, 632/22 nm_676/34 nm), FITC/TRITC (excitation_emission, 475/28 nm_594/45 nm), and DAPI/DAPI (excitation_emission, 380/18 nm_435/48 nm). Images were analyzed using the SoftWorks deconvolution software.

Immunofluorescence Cells were washed with cold phosphate-buffered saline (PBS) and fixed with 3.7% formaldehyde in PBS. For permeabilization, the cells were incubated in 0.1% Triton X-100 in PBS for 15 min at room temperature. The samples were washed three times with ice-cold PBS, followed by incubation with 2% BSA in PBS for 1 h at room temperature. Fixed cells on dish were exposed to the diluted primary antibody solution (ubiquitin; 1:300, PCYT2; 1:200) in PBS with 1% BSA and 3 μM BODIPY 493/503 (Thermo, D3922) at 4 °C overnight. The primary antibody was decanted and washed three times with PBS. Thereafter, a diluted anti-rabbit IgG-TRITC antibody (1:200) solution with 3 μM BODIPY 493/503 and Hoechst 33342 (2 μg/ml) was applied to the samples and incubated at room temperature for 1 h. After washing three times with PBS, fluorescence images were captured in PBS using DeltaVision Elite fluorescence microscopy (100× scale) using TRITC/TRITC, (excitation_emission, 542/27 nm_594/45 nm), FITC/FITC (excitation_emission, 475/28

nm_525/48nm), and DAPI/DAPI (excitation_emission, 380/18 nm_435/48 nm). Images were analyzed using the SoftWorks deconvolution software.

Fluorescent FFA Pulse-Chase experiments AML12 cells were incubated with 2 μM BODIPY 558/568 C12 (Thermo, D3835) in complete media for 21 h. Cells were then washed twice with complete media, incubated for additional 1 h. **SB2301** was treated for 24 h. For positive control, serum-starved (16 h) cells were prepared separately. Mitochondria were labeled with 100 nM MitoTracker DeepRed (Thermo, M22426) and LDs were labeled with 10 μM SF44 for 30 min simultaneously prior to fluorescence imaging. Live cell imaging was conducted within 2 h.

TS-FITGE Human hepatocellular carcinoma HepG2 cells were incubated in serum-free DMEM with 20 μM **SB2301** (0.2% (v/v) of DMSO in final concentration) for 1 h at 37 °C. Heat shock was applied to the cells for 3 min. The resulting cells were stabilized at 25 °C for 3 min, washed once with PBS, and resuspended in PBS containing 0.4% NP-40 and protease inhibitor. Cells were subjected to three freeze (liquid nitrogen)/thaw cycles for cell lysis. The cell lysate was clarified by centrifugation at 20000 g for 20 min at 4 °C. 50 mg of protein was precipitated, and the residual pellet was resuspended in 10 μl of labeling buffer (30 mM Tris-HCl at pH 8.6, 2 M thiourea, 7 M

urea, and 4% w/v CHAPS) with sonication. The soluble proteomes were mixed with 0.4 mM Cy3-NHS (for DMSO-treated group) or Cy5-NHS (for **SB2301**-treated group), and incubated at 4 °C for 45 min. The dye-conjugated proteomes were precipitated with cold acetone and resuspended in 75 μl of rehydration buffer (7 M urea, 2 M thiourea, 2% w/v CHAPS, 40 mM DTT, and 1% IPG buffer). DMSO-treated **SB2301**-treated samples were mixed, and 150 μl (75 μl for Cy3- and Cy5-labeled each) of proteomes was loaded on a 24-cm Immobiline Drystrip gel [GE Healthcare]. Isoelectric focusing was performed using Ettan IPGphor 3 [GE Healthcare] followed by 2-dimensional SDS-PAGE with an Ettan DALTsix system [GE Healthcare]. The gel was scanned using a Typhoon Trio [GE Healthcare]. For LCMS/MS, the gel was excised after silver staining.

CETSA Trypsinized HepG2 cells were incubated in serum-free DMEM media with the 20 μM compound (final 0.2% (v/v) DMSO concentration) for 1 h at 37 ºC. Heat shock applied to cell for 3 min and cells were stabilized at 25 ºC for 3 min. Wash cell with PBS once and resuspend cells with PBS containing 0.4% NP-40 and protease inhibitor. Lysis cells with freeze (liquid nitrogen)/thaw cycle, 3 times. Prepare soluble proteins and detect protein quantity with western blotting. (Primary antibody dilution/anti-ACSL4; 1:1000, anti-PCYT2; 1:1000, anti-IDH1; 1:1000, anti-WDR1; 1:200, anti-GAPDH; 1:2000)

SPR analysis The equilibrium dissociation constant (K_D) toward PCYT2 was determined by SPR using a Biacore T100 instrument [GE Healthcare]. The carboxyl group on the surface of the CM5 sensor chip was replaced with reactive succinimide ester using a combination of 1-ethyl-3-(3-dimethylaminopropyl)-carbodiimide (EDC) and N-hydroxysuccinimide (NHS) in flow cells 1 and 2. Human PCYT2 (Prospec, enz-221) was immobilized on flow cell 2 (10000 RU) through the formation of amide bonds by reacting with the resulting NHS ester. The remaining NHS ester on flow cells 1 and 2 was quenched via injection with 1 M ethanolamine-HCl (pH 8.0) solution. During the immobilization process, PBS was used as the running buffer. After immobilization, different concentrations of the compounds were injected for 60 s at a flow rate of 10 μL·min-1. At the same flow rate, the dissociation from the sensor surface was monitored for 300 s. For the running buffer, we used 1× PBS (pH 7.3) containing 3% DMSO and 0.05% P20. The binding events were measured at 25 °C. Data analysis was performed using the Biacore T100 Evaluation software [GE Healthcare]. Final sensorgrams were obtained after the elimination of responses from flow cell 1 and buffer-only control. The K_D was calculated by fitting the sensorgrams to a 1:1 binding model.

LD fractionation LDs were isolated from HepG2 cell (~108 cells) using LD isolation kits (Cell Biolabs, MET-5011) according to

the manufacturer's instructions. The membrane, cytosol, and LD fraction were collected for purity check. To separate the proteins and lipids from isolated LDs, 1 ml of chloroform/acetone (1:1, v/v) was added. The organic phase was collected for further phospholipid composition analysis. Repeat this process twice with the pellet to dissolve the lipids. After removing the organic phase, the pellet was dried at room temperature and resuspended with SDS sample buffer to prepare proteins for purity check.

LD size distribution by volume Dynamic light scattering data was obtained with a purified LDs in PMMA cuvette (Ratiolab, 2810100) by Malvern Zetasizer Nano-S. Dispersant and temperature were selected as water and 25 °C, respectively.

PE/PC ratio analysis To measure the amount of PE and PC in the lipid sample, the PE assay kit (Biovision, K499) and PC assay kit (Biovision, K576) were used. Extracted lipids from whole cell lysate or purified cellular LDs were prepared via solvent evaporation using a rotary evaporator. Dried lipids reconstituted with PE assay buffer and PC assay buffer were employed, according to the manufacturer's instructions, to measure each quantity.

LD volume and size distribution analysis Ten fluorescence images were captured at one point with 0.8 μm z-depth. Projected

images were generated using SoftWorks deconvolution software. Fifteen randomly selected images from each condition were analyzed using InCell Developer [GE Healthcare], and the diameters of all LDs present in the given image were quantified. Assuming that the LD is a perfect sphere, the volume of each lipid droplet was calculated using the relationship between the radius and volume ($V=4/3\ \pi r^3$). The LDs were divided into nine groups according to the length of the radius. The LD size distribution was calculated by dividing the sum of the volumes of LDs corresponding to each group by the sum of the volumes of total LDs.

Oxygen consumption rates (OCR) measurement AML12 cells were seeded on an Agilent Seahorse XFe24 plate and subsequently treated with **SB2301**. A sensor cartridge with Seahorse XF Calibrant (Agilent, 100840-000) was hydrated at 37 °C overnight in a non-CO2 incubator. OCR was measured in Seahorse XF DMEM (Agilent, 103757-100) containing 17 mM glucose (Agilent, 103577-100), 2.5 mM glutamine (Agilent, 103579-100), and 0.5 mM pyruvate (Agilent, 103578-100) in response to 1.5 μM oligomycin, 1 μM fluorocarbonylcyanide phenylhydrazone (FCCP), and 0.5 μM rotenone + antimycin A (Seahorse XF Cell Mito Stress Test Kit, 103015-100) with Seahorse XFe24 [Agilent].

PCYT2 enzymatic assay PCYT2 activity was assayed as

described previously with minor modification.1 Briefly, prepare a 50 μl mixture of 20 mM Tris-HCl buffer with pH 7.8, 5 mM DTT, 10 mM MgCl2, 650 μM phosphoethanolamine, and CTP with various concentration. Then the reaction mixture was incubated with 0.1 μg of purified PCYT2 at 37 ºC for 3 min. Reactions were terminated by boiling for 2 min. The concentration of product (pyrophosphate) was measured by pyrophosphate assay kit (Lonza, LT07-610), and the reaction rate was calculated. DMSO and **SB2301** were added at the indicated concentration in the reaction mixture.

si-RNA transfection 20 μM of si-RNA was applied to HepG2 cells for 48 h with Lipofectamine RNAiMAX (Invitrogen, 13778-100) following manufacture's protocols.

[si-RNA sequences]

Gene	Sense	antisense
Atg5 (Ambion, s18158)	AUG AGC UUC AAU UGC AUC CTT	AAG GAU GCA AUU GAA GCU CAU
Acsl4 (Bioneer, 2182-1)	CA CAC ACU UCG ACU CAC UT	UA GUG AGU CGA AGU GUG UG
Pcyt2 (Bioneer, 5833-2)	CU CAU CGU CCA GCG GAU CA	UG AUC CGC UGG ACG AUG AG
Idh1 (Bioneer, 3417-1)	GC UGU GCA UUA AAC UUG CA	UG CAA GUU UAA UGC ACA GC

3. Results and discussion

3.1. Image-based high throughput screening and hit compound selection.

To discover the novel compound that exhibits LD reducing activity, Dr. Jinjoo Jung used image-based high throughput screening system. Thousands of drug-like small molecules synthesized by pDOS (privileged substructure-based diversity-oriented synthesis) strategy were subjected to screening. She used a specific LD staining fluorescent dye, SF44, to visualize the LDs present in HeLa cells. Using an image analysis tool, she quantified the size and number of LDs from images and evaluated the activity of each compound. As a result, she obtained several compounds having LD reducing activity from the pDOS library (**Fig. 1**). Given the structure and activity relationship, the most potent compound, **SB2301**, was selected as a final hit compound (**Table 1**, **Fig. 2A**).

SB2301 showed dose-dependent LD reduction activity on HeLa cells with 4.4 μM of IC_{50} upon 24 h treatment (**Fig. 2B, 2C**) without severe cytotoxicity (**Fig. 2D**). Our research goal is drug discovery for NAFLD treatment, so we tested whether **SB2301** has an LD-reducing effect on the hepatic cell lines. Fortunately, **SB2301** maintained its LD reducing activity on hepatic cell lines such as HepG2 and AML12 (**Fig. 3**). Thus, further mechanistic studies were conducted with hepatocytes.

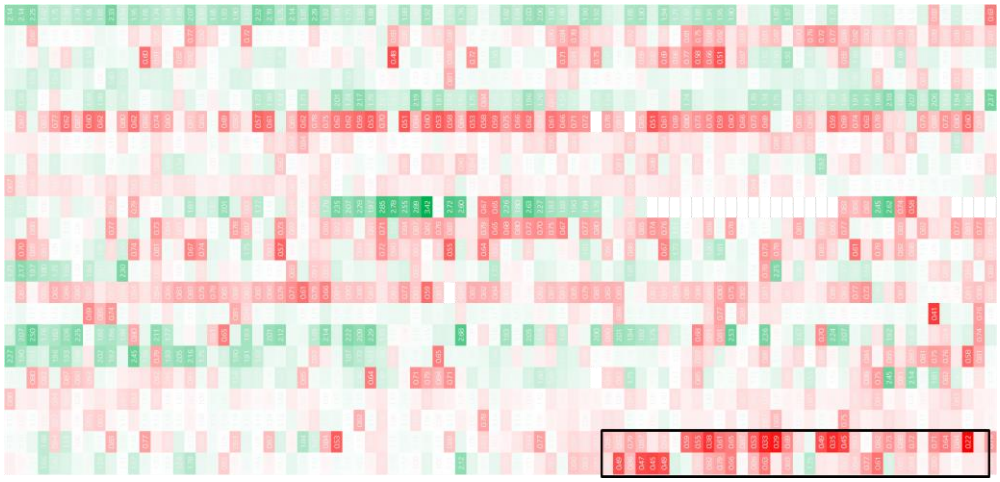

Figure 1. Image-based LD monitoring high-content screening results. HeLa cells were treated with in-house library compounds at 10 μM for 24 h. LDs counts were normalized over DMSO control. The red and green colors indicate that the number of LDs decreases and increases after compound treatment, respectively.

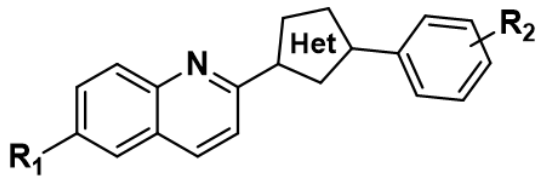

Cpd.	R_1	Het	R_2	LD reduction (%)	LD reduction (IC_{50}, μM)
1	3-Hydroxyphenyl	1,4-triazole	2-OCH_3	50.0	6.7
2[a,b]	3-Hydroxyphenyl	1,4-triazole	3-OCH_3	29.8	10.2
3	3-Hydroxyphenyl	1,4-triazole	4-OCH_3	19.0	3.7
4	3-Hydroxyphenyl	1,4-triazole	2-CF_3	64.5	4.4
5[b]	3-Hydroxyphenyl	1,4-triazole	3-CF_3	46.6	N/A
6	3-Hydroxyphenyl	1,4-triazole	4-CF_3	35.9	32.0
7	3-Hydroxyphenyl	1,4-triazole	2-CN	30.4	14.8
8[a]	3-Hydroxyphenyl	1,4-triazole	3-CN	-7.1	27.6
9[b]	3-Hydroxyphenyl	1,4-triazole	4-CN	-3.9	N/A
10[a]	3-Hydroxyphenyl	1,4-triazole	2-Cl	2.7	10.1
11	3-Hydroxyphenyl	1,4-triazole	3-F	19.2	20.6
12[a]	3-Hydroxyphenyl	1,4-triazole	4-Br	36.8	4.7
13	3-Hydroxyphenyl	1,4-triazole	2-OH	12.7	11.6
14[a]	3-Hydroxyphenyl	1,4-triazole	2-NO_2	48.5	7.9
15[b]	3-Hydroxyphenyl	1,4-triazole	2-CH_3	40.9	2.6
16[b]	3-Hydroxyphenyl	1,4-triazole	H	7.0	>1000
17[b]	H	1,4-triazole	2-CF_3	-5.6	>1000
18[b]	3-Hydroxyphenyl	isoxazole	2-CF_3	42.3	9.5
19	H	isoxazole	2-CF_3	-6.7	40.0
20[a]	3-Hydroxyphenyl	isoxazole	H	47.6	26.0

[a] Cell's morphology was changed
[b] Compound was insoluble in media at 10 μM
N/A; Not applicable

Table 1. Structure and activity relationship results. Each compound was treated on HeLa cells for 24 h. **Compound 4** was selected as a final hit compound (**SB2301**), and **compound 10** was used as a negative compound in the following study.

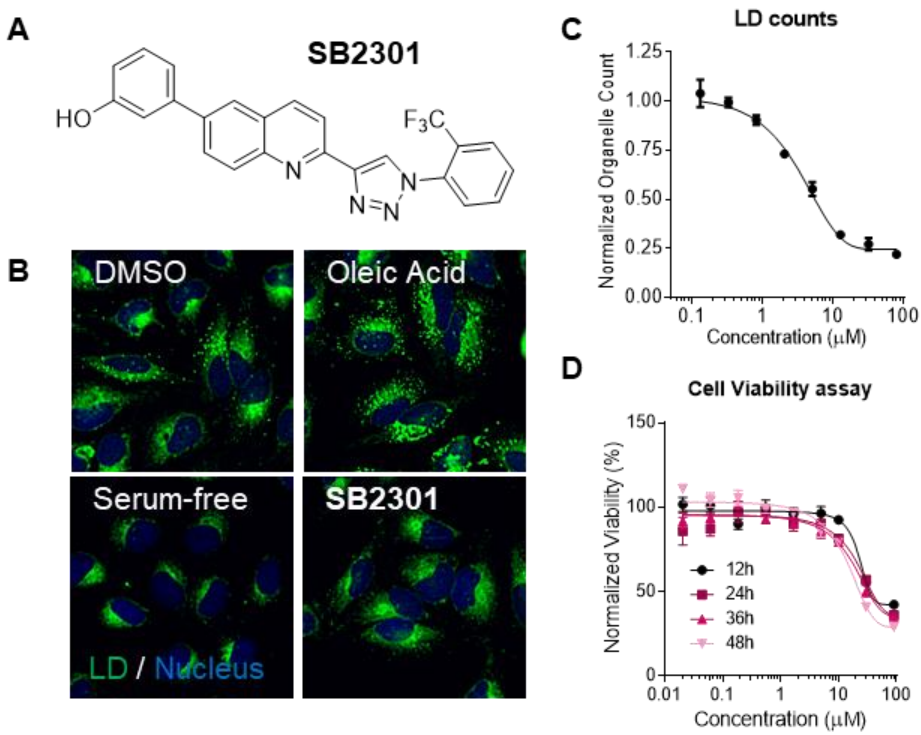

Figure 2. SB2301 showed LD reduction activity without severe cytotoxicity. (A) Chemical structure of **SB2301 (B)** Representative LD image of each condition. 10 μM of oleic acid, and 5 μM of **SB2301** were treated on HeLa cells for 24 h. **(C)** The quantification of cellular LD counts upon **SB2301** treatment with various doses for 24 h on HeLa cells. All data were shown as the mean ± s.d. (D) Cell viability assay results upon **SB2301** treatment. All data were shown as the mean ± s.d

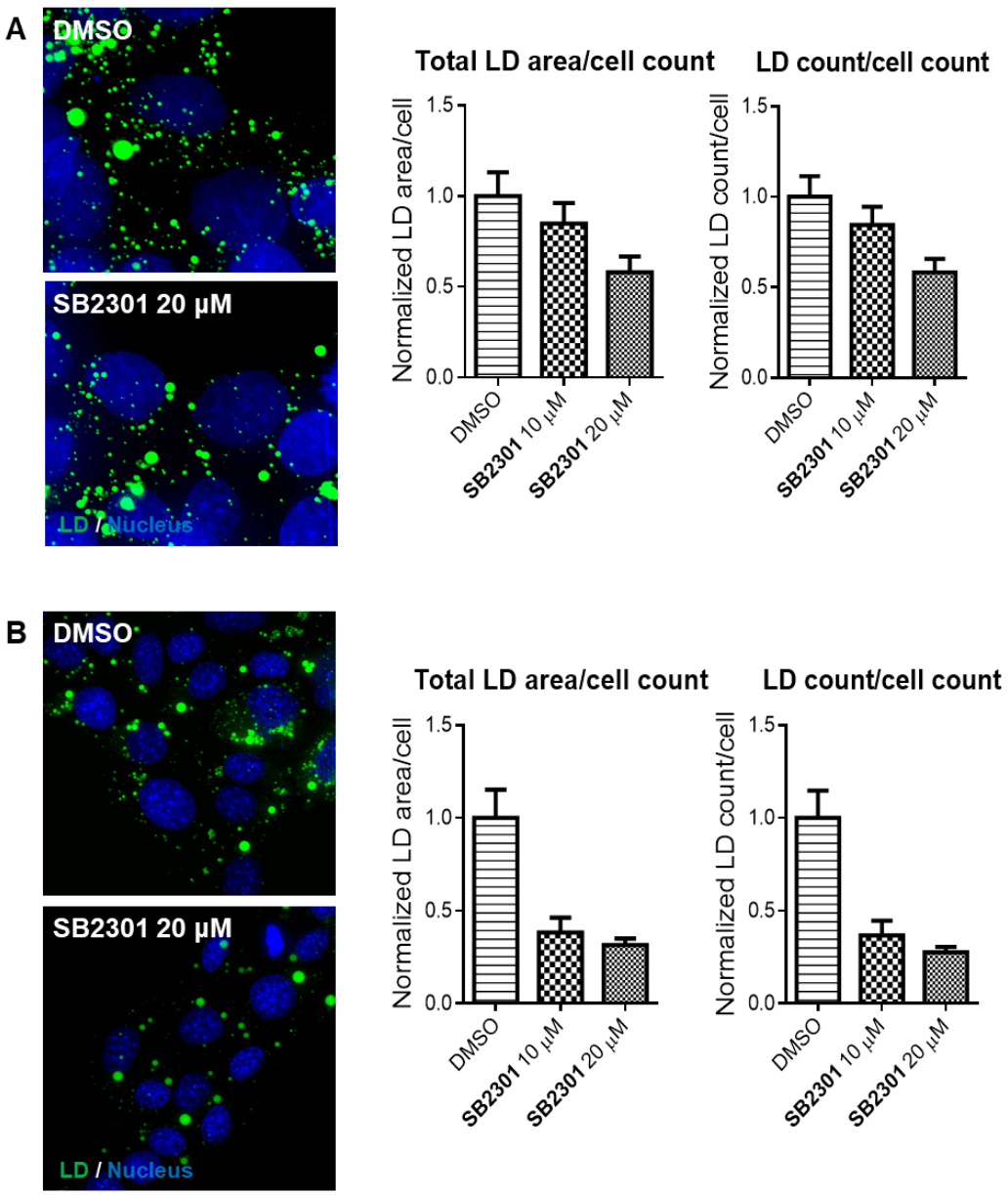

Figure 3. SB2301 showed LD reduction activity on hepatic cell lines.

Representative LD images and quantification results **(A)** on HepG2 cells and **(B)** AML12 cells. **SB2301** was treated on cells for 24 h then LD fluorescence images were obtained. All data were shown as the mean ± s.d

3.2. SB2301 induces lipid droplet coalescence.

The formation of large LD (called mega LD) was observed upon **SB2301** treatment. Therefore, I classified the LD degrading process by **SB2301** into two phases. In the first phase, mega LDs increased over time, reaching its maximum number after 18 hours. In the second phase, mega LDs started to disappear, and they were completely removed after 48 hours (**Fig. 4A**).

To explain the formation and disappearance of mega LDs, I introduced the concept of *degree of contribution*. First, I measured the radius of all LDs in each image and calculated their volume. Then, LDs were classified into nine groups according to their size. Finally, the contribution of each group to the total volume was calculated and defined as the *degree of contribution* (**Fig. 4B**). By introducing this parameter, I was able to quantify this phenomenon through the bar graph. As shown in **Fig. 4C** and **Fig. 4D**, the blue bar graph shifted to the right and returned to its original state. Although there was a difference in time scale between cell lines, this phenomenon was also observed in AML12 cell line (**Fig. 5**).

A

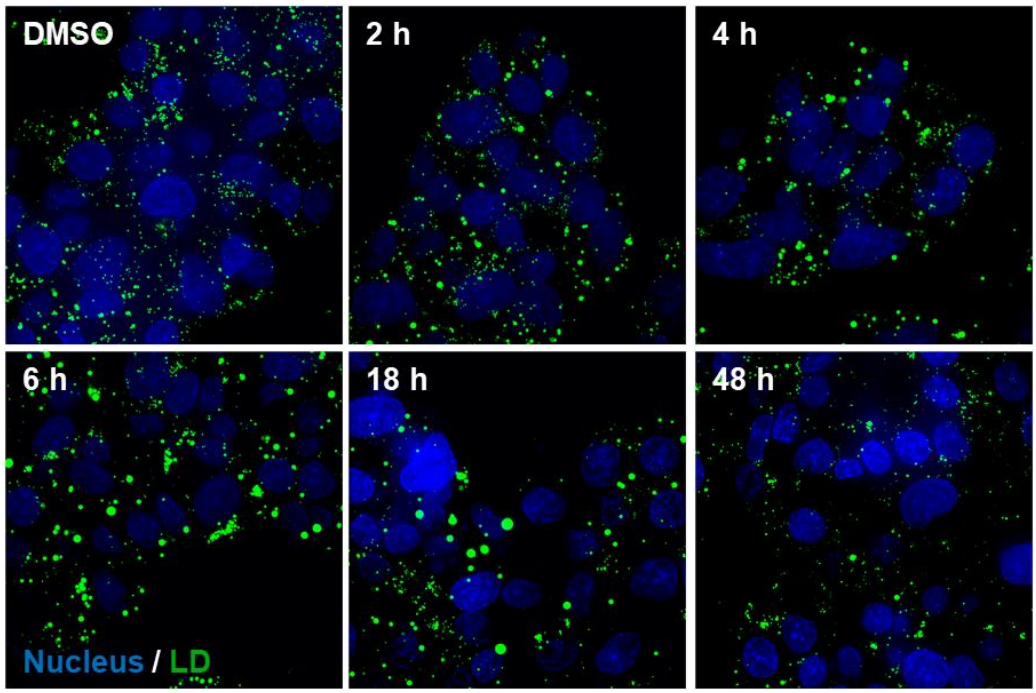

B

$$(Degree\ of\ Contribution)_i = \frac{(Lipid\ droplet\ volume)_i}{\sum(Lipid\ droplet\ volume)_i}$$

C

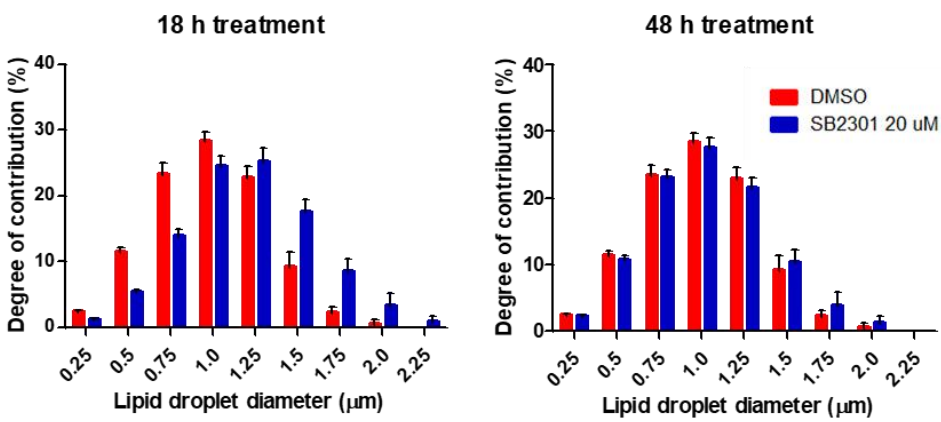

D

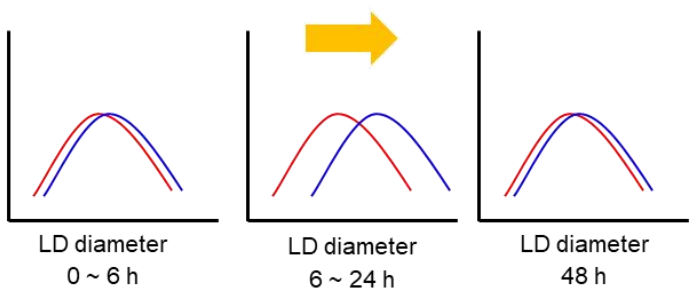

Figure 4. SB2301 induces LD coalescence on HepG2 cells.

(A) Representative LD images of each time point. 20 μM of **SB2301** was treated on HepG2 cells. **(B)** The definition of *degree of contribution*. **(C)** Calculated *degree of contribution* of each time point. The blue bars indicate **SB2301** treated condition, and the red bars indicate DMSO treated condition. All data were shown as the mean ± s.d **(D)** Schematic figure to show the change of *degree of contribution* upon **SB2301** treatment.

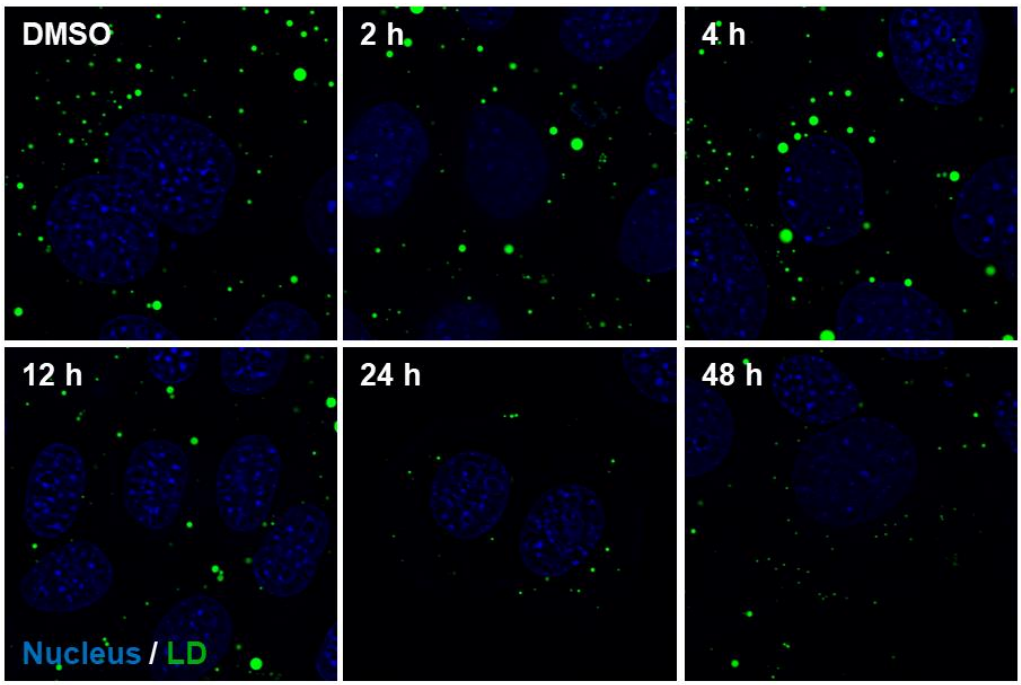

Figure 5. SB2301 induces LD coalescence on AML12 cells.

Representative LD images of each time point. 20 μM of **SB2301** was treated on AML12 cells. Mega LD formation and disappearance time points are earlier than HepG2 cells.

3.3. Mega LD activates lipophagy and degrades itself.

It is necessary to understand mega LD formation and disappearance mechanisms for explaining the mode of action of **SB2301**. Among these two phenomena, first, I focused on the disappearance of mega LD. I thought autophagy is the most plausible mechanism to degrade mega LDs because it is a major clearance mechanism that removes damaged organelles or aggregated proteins. A representative example is a mitophagy. Mitophagy is a type of selective autophagy, controlling mitochondria quality by removing dysfunctional mitochondria. Damaged mitochondria could not maintain membrane potential, and then they undergo ubiquitination. Then ubiquitinated mitochondria are recognized by autophagy machinery and encapsulated into autophagosomes. Therefore, I hypothesized that mega LDs are recognized as abnormal organelles, like impaired mitochondria, and removed by autophagy. To demonstrate this hypothesis, I conducted several experiments to show a relationship between mega LD degradation and autophagy activation.

First, I verified whether **SB2301** activates autophagy by immunoblotting LC3 protein. LC3 is an essential protein for autophagosome formation, and its conversion is highly related to autophagy activation. When autophagosomes are formed, LC3Ⅰ is anchored to phosphatidylethanolamine (PE) and changes to LC3Ⅱ. In western blotting analysis, the conversion of LC3Ⅰ to LC3Ⅱ was observed upon **SB2301** treatment in a dose-dependent manner (**Fig.**

6A) and in a time-course study (**Fig. 6B**). Interestingly, LC3 conversion was observed after mega LD formation. Then I tested whether **SB2301** mediated autophagic full flux went ahead by co-treatment with bafilomycin A1. Bafilomycin A1 is known as an inhibitor of vacuolar-type H^+-ATPase. It inhibits lysosome acidification, preventing fusion between autophagosome and lysosome. As shown in **Fig. 6C**, co-treatment **SB2301** with bafilomycin A1 showed a much stronger LC3 conversion than bafilomycin A1 sole treatment. To cross-confirm the effects of **SB2301** on autophagic flux, the mCherry-GFP-LC3 experiment, a method for observing autophagic flux in live cells, was carried out. The intrinsic fluorescence of GFP is quenched when exposed to acidic conditions. However, in the case of mCherry, the intrinsic fluorescence is maintained.[24] Due to these properties, mCherry-GFP-LC3 puncta is observed as yellow in a neutral environment (autophagosome) and red in an acidic environment (autolysosome). Rapamycin, a well-known autophagy inducer, increased the red puncta, and Bafilomycin A1 increased yellow puncta in this experiment. Increasing red puncta was also observed upon **SB2301** treatment (**Fig. 6D**). Through these data, I concluded **SB2301** increases autophagic flux.

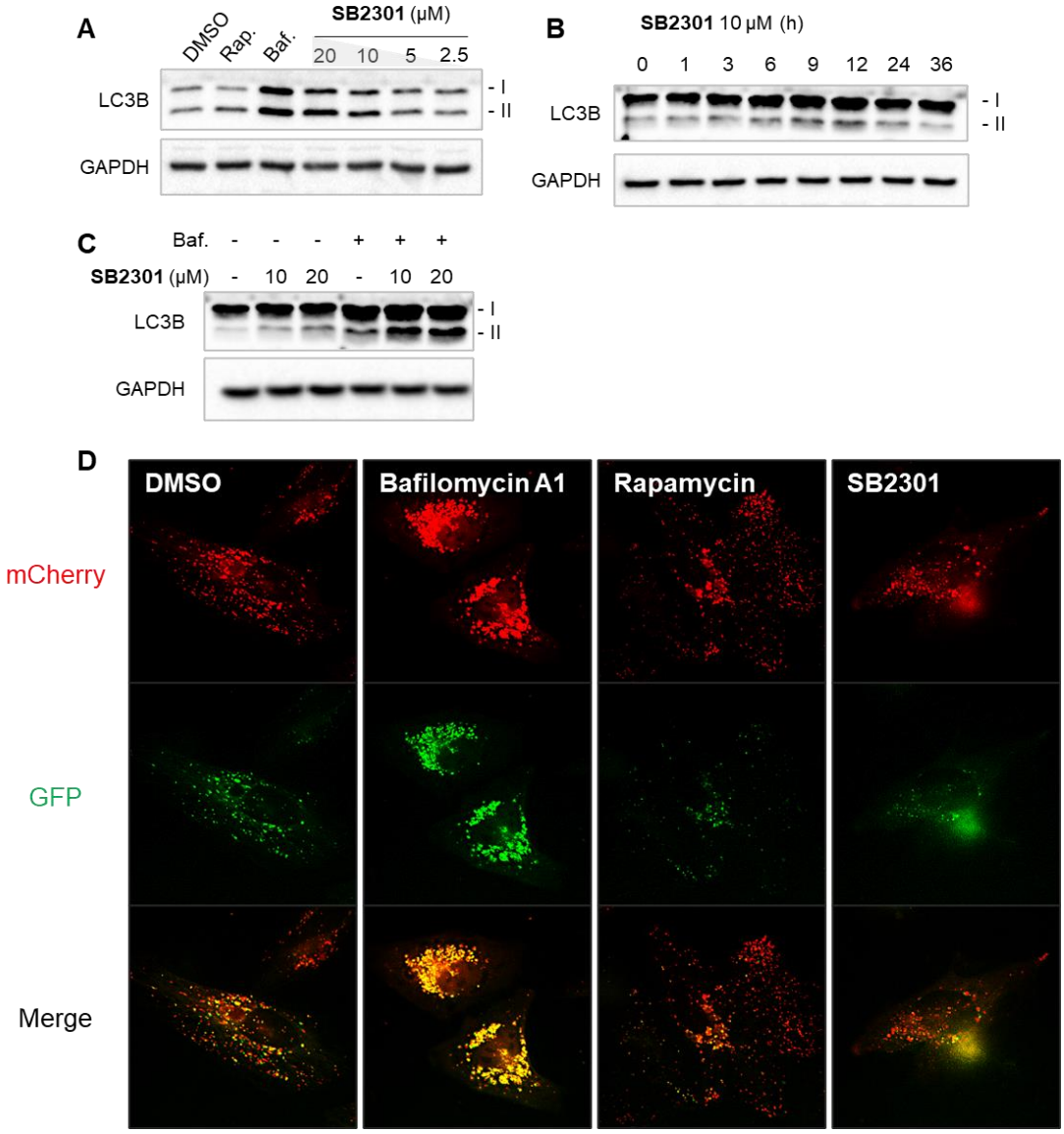

Figure 6. Autophagy activation by SB2301. (A) HepG2 cells were treated with **SB2301** for 12 h at various concentrations. Rapamycin (Rap) and Bafilomycin A1 (Baf) were treated at 2 μM and 20 nM, respectively. **(B)** HepG2 cells were treated with 10 μM of **SB2301** in time-course. **(C)** HepG2 cells were treated with **SB2301**, and 5 nM of Baf for 6 h. **(D)** HeLa cells were transfected with mCherry-GFP-LC3 plasmid and treated with 500 nM of Rap, 20 nM of Baf or 5 μM of **SB2301** for 16 h.

Next, I investigated the colocalization between LD and autophagosome to establish the relationship between mega LD degradation and autophagy. LC3 is a maker to represent the location of the autophagosome.[18] It highly colocalized with LDs upon **SB2301** treatment (**Fig. 7**). In addition, the colocalization of lysosomes and LDs also increased after **SB2301** treatment (**Fig. 8**). To cross-confirm that autophagy removes mega LDs, I tested the effect of **SB2301** on ATG5 knockdown cells. ATG5 is involved in early-stage autophagy, making a complex with ATG12.[25] ATG5-ATG12 complex acts as an E3-like enzyme and affects LC3 lipidation.[26] Thus, ATG5 knockdown can block autophagy (**Fig. 9A**). As shown in **Fig. 9B**, mega LD formation was still observed under ATG5 knockdown condition. In contrast, mega LD was not degraded and maintained even after 48 hours of **SB2301** treatment. These data demonstrated that autophagy, especially lipophagy, is essential for mega LD degradation.

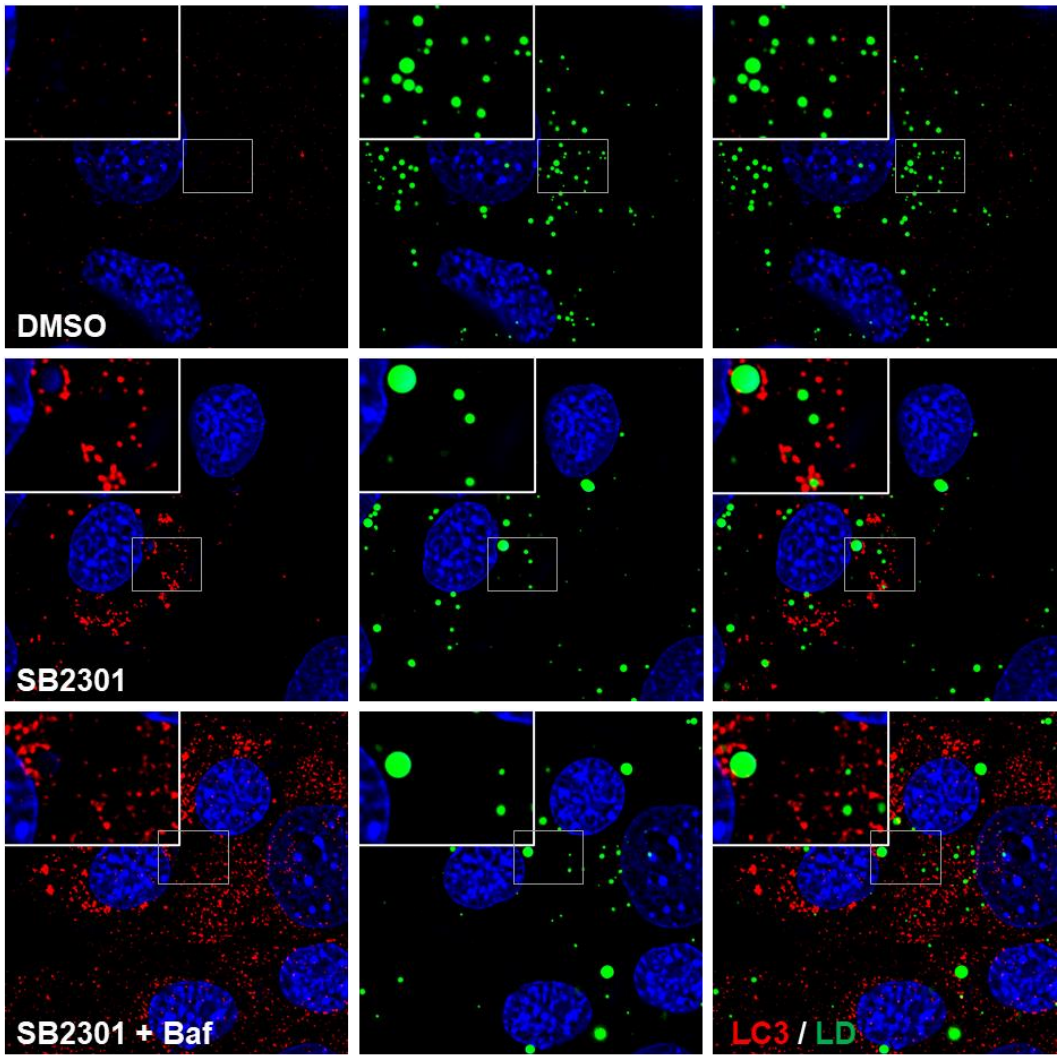

Figure 7. Colocalization between LC3 and LD is increased upon SB2301 treatment. Representative images of each condition. 20 μM of **SB2301** and 5 nM of bafilomycin A1 were treated on AML12 cells for 6 h.

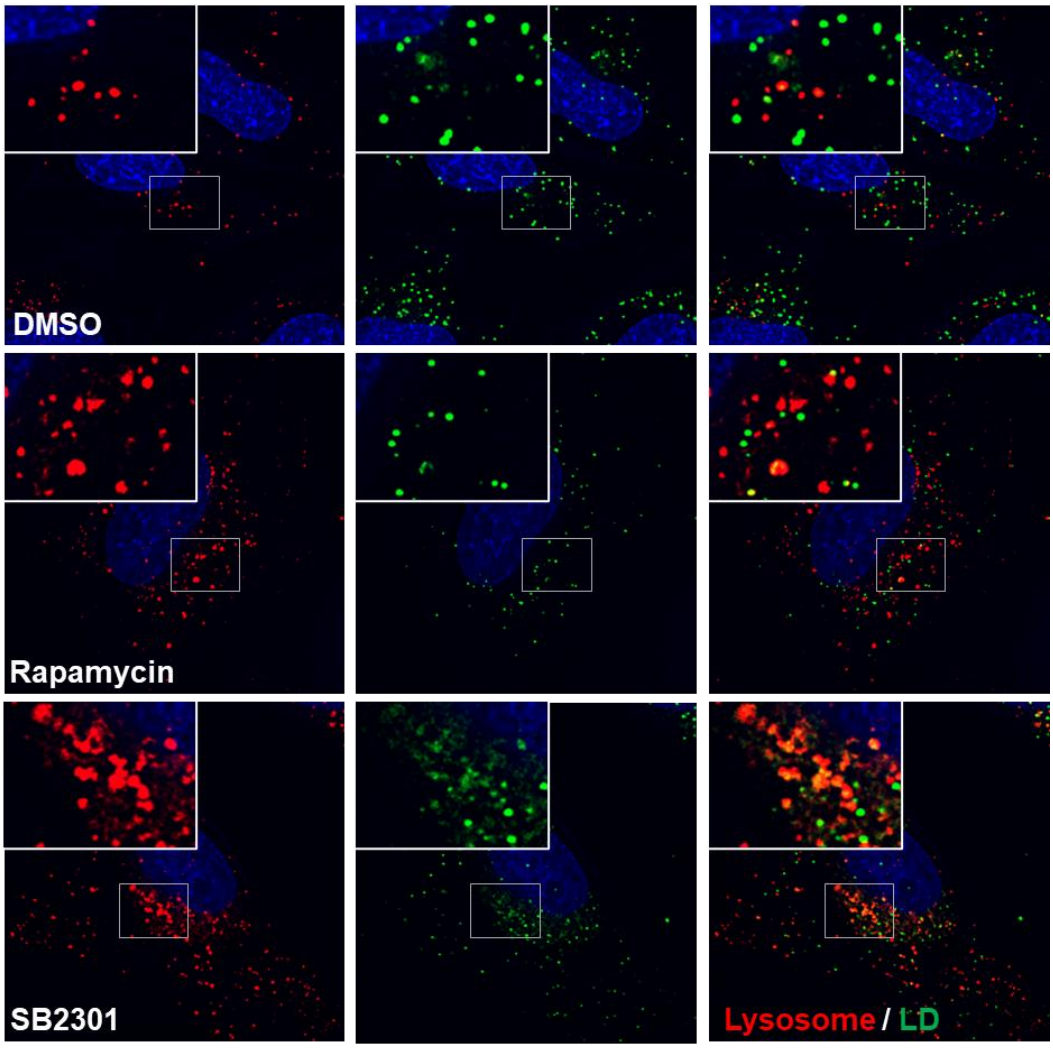

Figure 8. Colocalization between lysosome and LD is increased upon SB2301 treatment. Representative images of each condition. 5 μM of **SB2301** and 1 μM of rapamycin were treated on HeLa cells for 12 h.

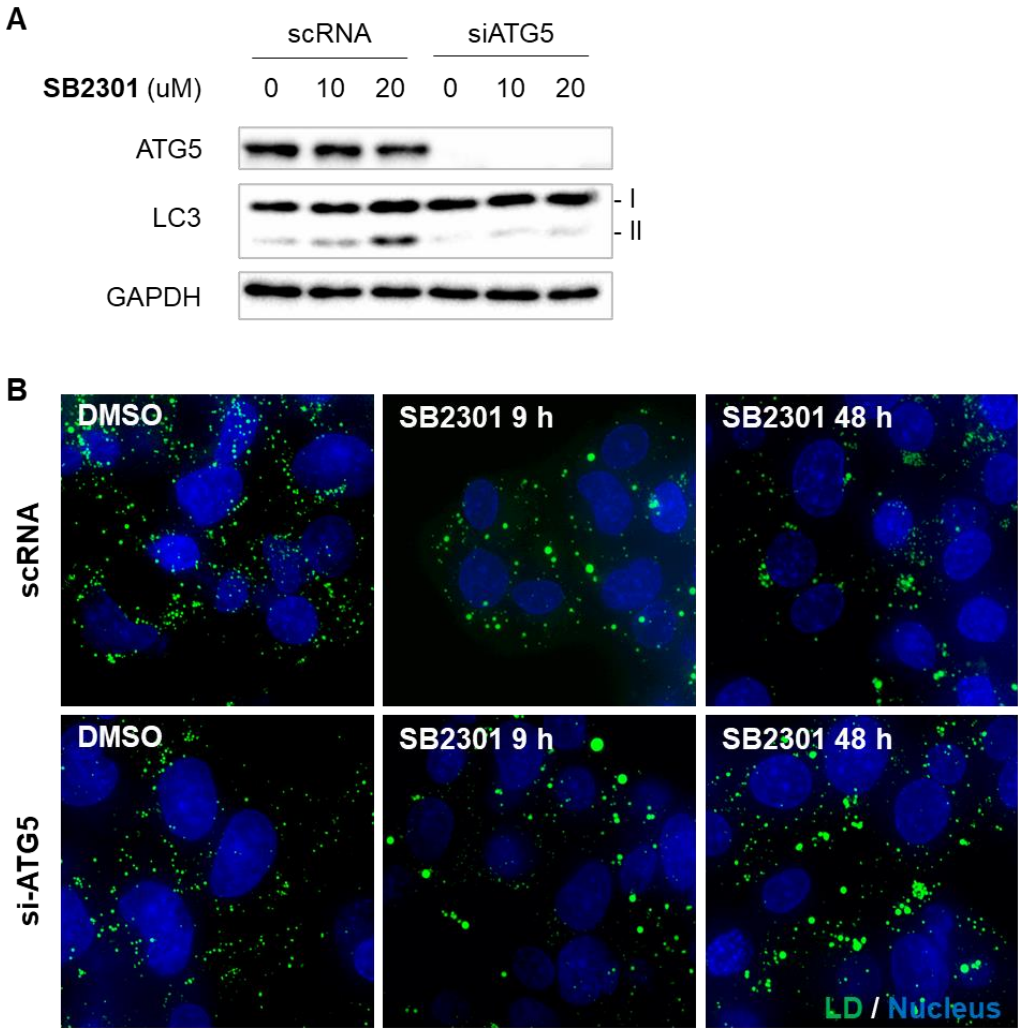

Figure 9. Autophagy activation is essential for degrading mega LDs.

(A) Immunoblot results of ATG5 and LC3. **SB2301** was treated on ATG5 knockdown HepG2 cells for 9 h. **(B)** Representative LD images of each condition. Degradation of mega LD is blocked by ATG5 knockdown.

Finally, I performed immunofluorescence to elucidate how mega LDs are recognized and eliminated by the autophagy machinery. Many reports have revealed that ubiquitination is involved in recognizing selective autophagy cargos,[27] such as mitochondria,[28,29] pathogen,[30] and protein aggregates.[31] Taking into account these reports, I hypothesized that ubiquitination plays an important role in the degradation of mega LDs. As expected, LD ubiquitination significantly increased after **SB2301** treatment (**Fig. 10A**). The ratio of ubiquitin over LD signal was higher in the **SB2301** treated condition than DMSO control (**Fig. 10B**). In addition, the ubiquitination of the LD proteome increased significantly after **SB2301** treatment **(Fig. 10C)**. Furthermore, Rab7 protein, a central regulator of hepatocellular lipophagy,[32] was recruited to LD surface upon **SB2301** treatment. Based on this result, I concluded that mega LDs are recognized as an abnormal organelle, become ubiquitinated, and removed by the lipophagy process.

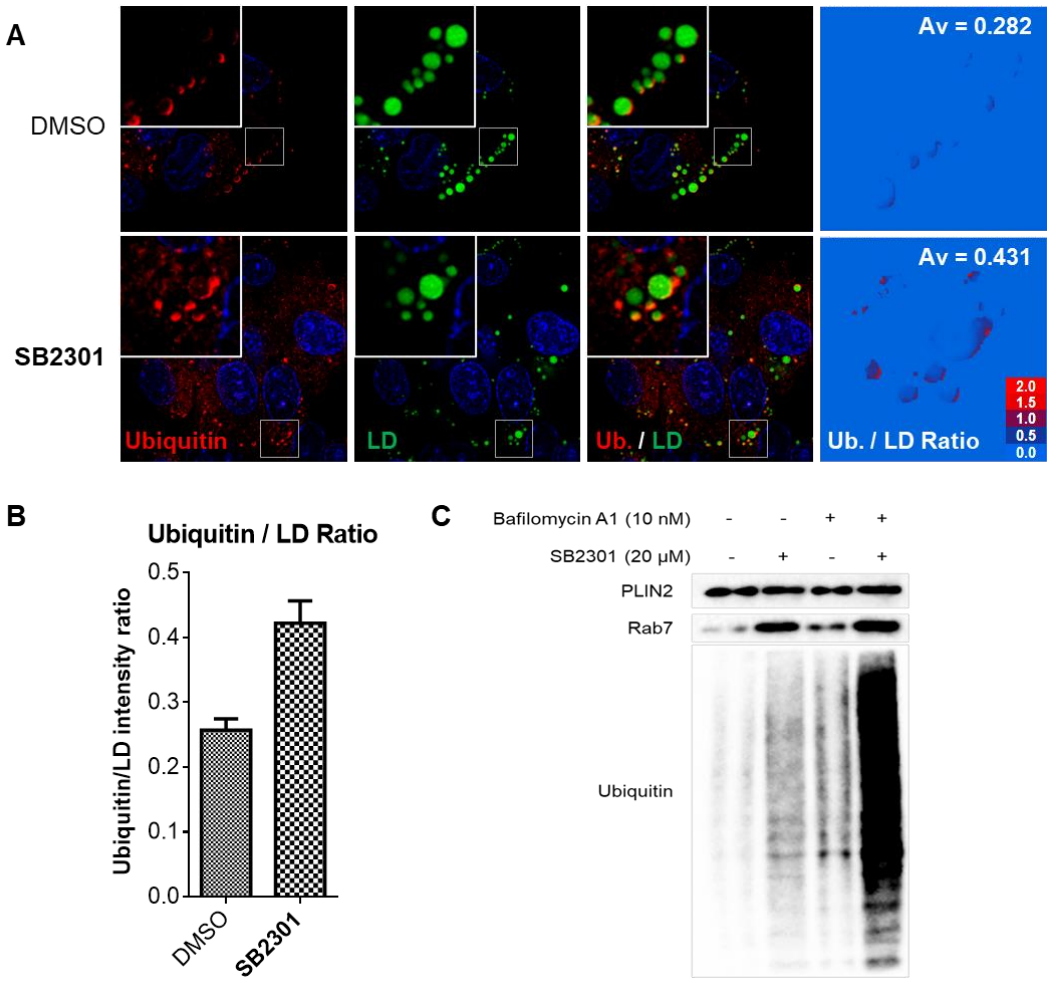

Figure 10. SB2301 induces LD ubiquitination. (A) Representative images of each condition. 10 μM of **SB2301** was treated on HepG2 cells for 12 h. **(B)** Pearson's correlation coefficient was calculated between ubiquitin and LD. **(C)** Western blot analysis with LD proteome, which purified from HepG2 cells. Each compound was treated for 12 h on HepG2 cells, and then LDs were isolated to obtain the LD proteome.

3.4. SB2301 increases lipid metabolism.

When the lipophagy is activated, free fatty acids are released from the lysosome to cytosol. Then cells rapidly remove them to avoid lipotoxicity. Thus, released free fatty acids are used as an energy source through beta-oxidation.[3] I carried out several experiments to confirm that **SB2301** increases lipid metabolism by inducing lipophagy.

First of all, I observed that mitochondria fission occurred and returned to original mitochondria morphology via time-course imaging (**Fig. 11**). Mitochondria fission is a representative phenotype caused by lipotoxicity.[5,8] As shown in **Fig. 11A**, mitochondria morphology did not change until mega LDs formed. However, when mega LDs started to disappear, mitochondria fission occurred. These results suggest that **SB2301** induces mitochondria fission via increasing free fatty acid concentration. In addition, with the restoration of mitochondria morphology, I hypothesized that released free fatty acids are rapidly degraded by beta-oxidation.

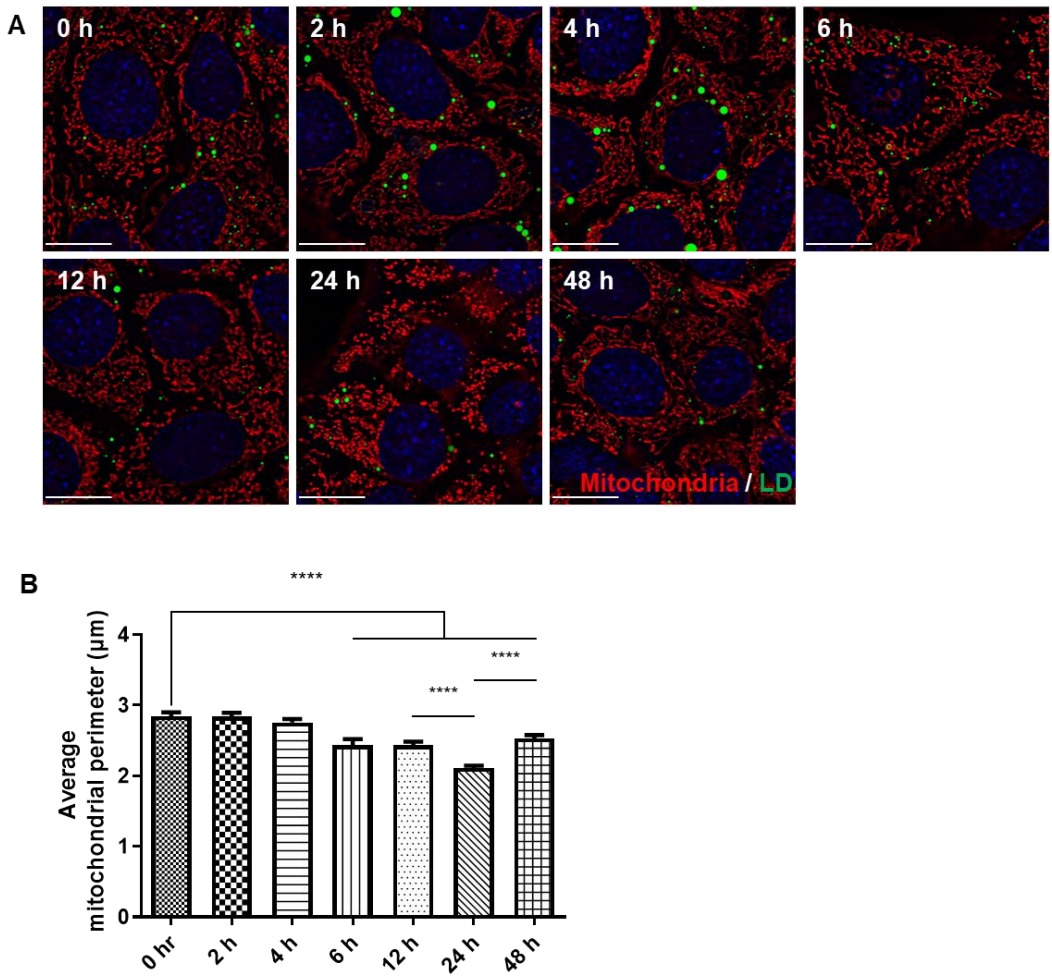

Figure 11. SB2301 induces mitochondria fission. (A) Representative mitochondria images of each time point. 20 μM of **SB2301** was treated on AML12 cells. **(B)** Quantification results of the average mitochondrial perimeter. All data were shown as the mean ± s.d

Next, I measured the oxygen consumption rate in mitochondria to prove whether **SB2301** increases beta-oxidation. The Seahorse XF Cell Mito Stress Test, the gold standard assay, was used to measure oxygen consumption rate change upon **SB2301** treatment. The spare respiratory capacity is known to be determined by substrate supply and oxidation.[33] As expected, the spare respiratory capacity increased after **SB2301** treatment (**Fig. 12A**). Thus, increment of spare respiratory capacity is strong evidence to supports increment of beta-oxidation.

Finally, I performed free fatty acid pulse and chase assay to measure the amount of free fatty acids in mitochondria. In this assay, a free fatty acid analog called BODIPY-C12 was used. It consists of two parts, BODIPY-dye and dodecanoic acid (C12). Due to BODIPY-dye is attached to the tail of dodecanoic acid, I could track the location of free fatty acids with fluorescence signal. BODIPY-C12 works like natural FFAs in the cell, so it is usually stored in LDs. However, when cells utilize lipids as an energy source, BODIPY-C12 moves to mitochondria for beta-oxidation. As shown in **Fig. 12B**, **SB2301** treatment increased free fatty acid translocation from LDs to mitochondria, like serum-free condition. These results show that the increment in oxygen consumption rate was due to the movement of free fatty acids to mitochondria.

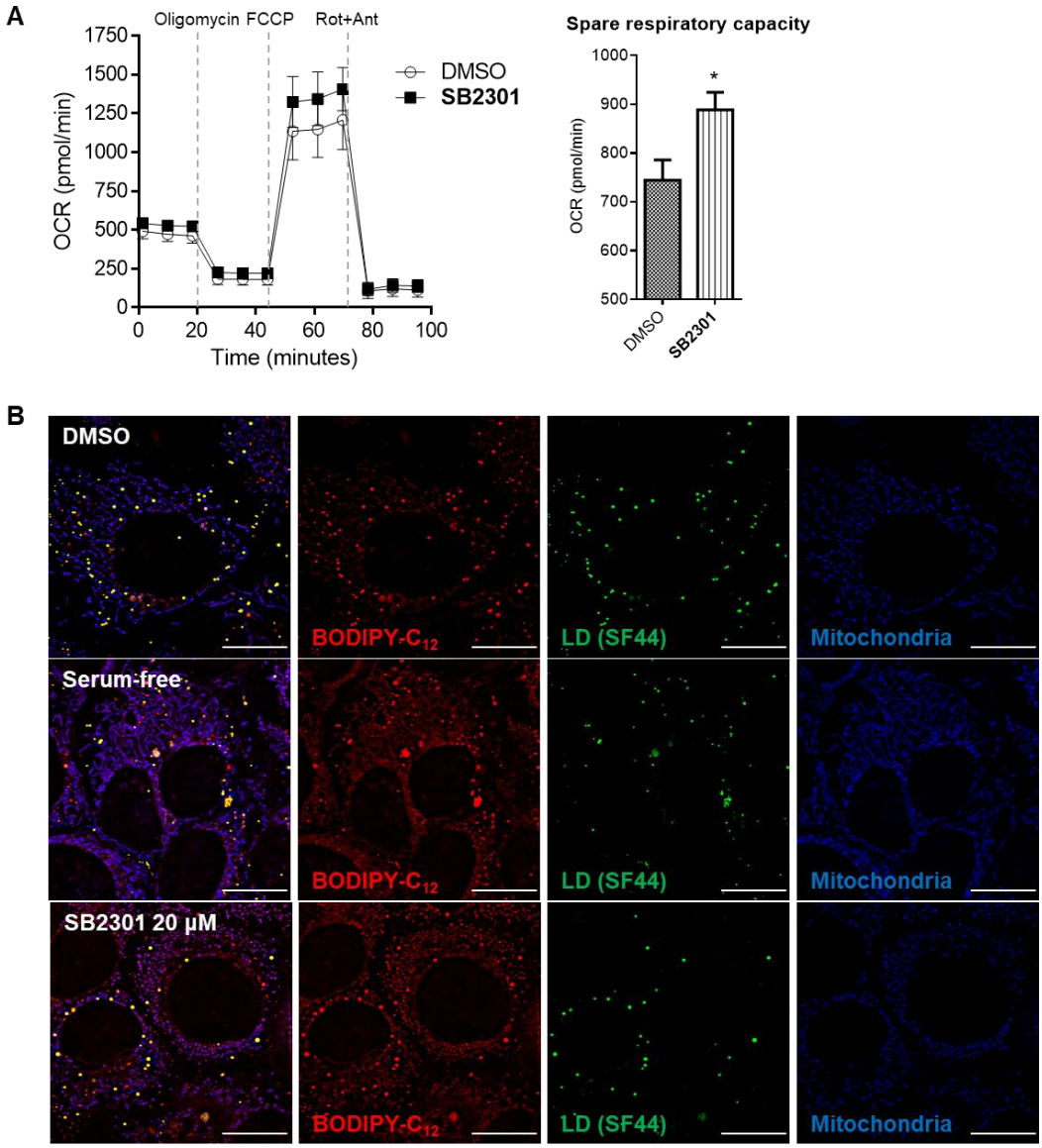

Figure 12. SB2301 increases lipid metabolism through lipophagy. (A) The results of Seahorse XF Cell Mito Stress Test. 20 μM of **SB2301** was treated on AML12 cells for 24 h. All data were shown as the mean ± s.d **(B)** Representative images of free fatty acid pulse and chase assay. **SB2301** was treated on AML12 cells for 24 h.

3.5. Target identification.

Target identification of **SB2301** is crucial to understand mega LD formation. For target identification, Dr. Jinjoo Jung and I used TS-FITGE (thermal stability shift-based fluorescence difference in two-dimensional gel electrophoresis) method. TS-FITGE is label-free target identification method and is based on the thermal stability shift of protein after compound engagement.[34] Proteins with increased thermal stability due to **SB2301** engagement appear red spots on TS-FITGE, while proteins with decreased thermal stability are shown as green spots. As shown in **Fig. 13**, I discovered seven red and two green spots, and each spot was identified through mass spectrometry (**Table 2**).

Among the target protein lists, we chose three proteins that function highly related to lipid metabolism. PCYT2 (Ethanolamine-phosphate cytidylyltransferase), ACSL4 (Long-chain-fatty-acid-CoA ligase 4), and IDH1(Isocitrate dehydrogenase [NADP] cytoplasmic) were selected, and cellular thermal shift assay (CETSA) was performed with these proteins (**Fig. 14A**). ACSL4 and PCYT2 showed thermal stability shift on **SB2301** treated condition. However, ACSL4 also showed thermal stability shift on negative compound (**10**) treated condition. In addition, for the loss of function study, I used si-RNAs to knockdown each target protein candidate (**Fig. 14B**). Only PCYT2 knockdown condition showed significant changes in LD count. Thus, I selected PCYT2 as the final target protein.

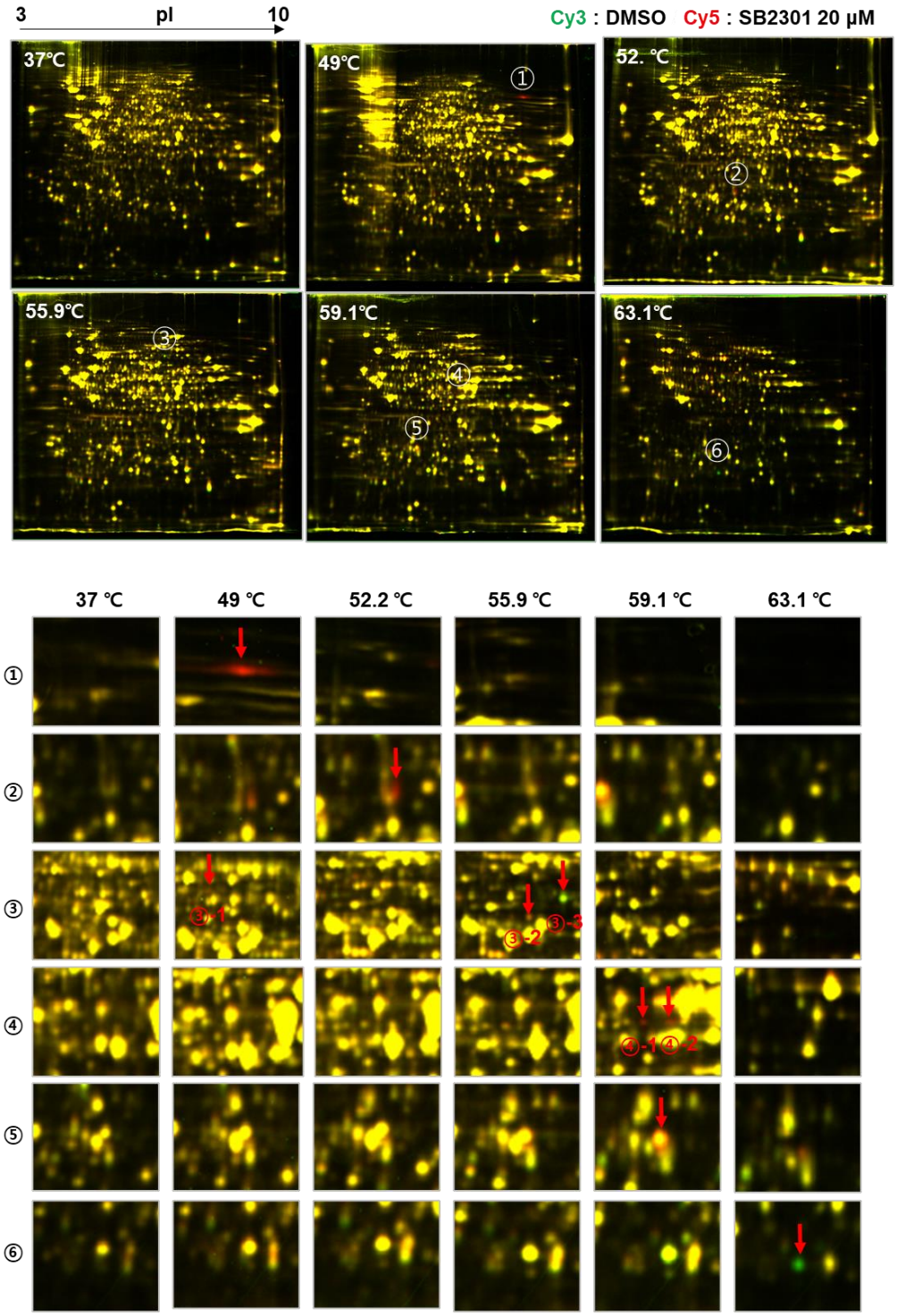

Figure 13. TS-FITGE results. 20 μM of **SB2301** was treated on HepG2 cells for 1 h. Seven red and two green spots were observed.

Spot No.	Match to	Molecular Weight	Mascot Score	Queries matched	Sequence Coverage (%)	Protein
①	ACSL4_HUMAN	79137	428	47	37	Long-chain-fatty-acid--CoA ligase 4
	DDX17_HUMAN	72326	278	21	30	Probable ATP-dependent RNA helicase DDX17
	DHB4_HUMAN	79636	101	7	9	Peroxisomal multifunctional enzyme type 2
	LDHA_HUMAN	36665	98	3	9	L-lactate dehydrogenase A chain
②	ST1A1_HUMAN	34175	165	24	20	Sulfotransferase 1A1
③-1	ERG7_HUMAN	83255	321	19	25	Lanosterol synthase
	ALBU_HUMAN	69321	82	5	6	Serum albumin precursor
③-2	PRDX3_HUMAN	27675	181	11	20	Thioredoxin-dependent peroxide reductase, mitochondrial precursor
③-3	WDR1_HUMAN	66152	345	30	27	WD repeat protein 1
④-1	PAPS1_HUMAN	70788	949	73	36	Bifunctional 3'-phosphoadenosine 5'-phosphosulfate synthetase 1
④-2	PCY2_HUMAN	43808	541	48	44	Ethanolamine-phosphate cytidylyltransferase
	PRS8_HUMAN	45597	96	2	5	26S protease regulatory subunit 8
⑤	PCY2_HUMAN	43808	654	43	44	Ethanolamine-phosphate cytidylyltransferase
	IDHC_HUMAN	46630	480	31	37	Isocitrate dehydrogenase [NADP] cytoplasmic
⑥	PRDX3_HUMAN	27675	1815	169	41	Thioredoxin-dependent peroxide reductase, mitochondrial precursor

Table 2. LC-MS/MS results. The nine spots from TS-FITGE were identified with LC-MS/MS.

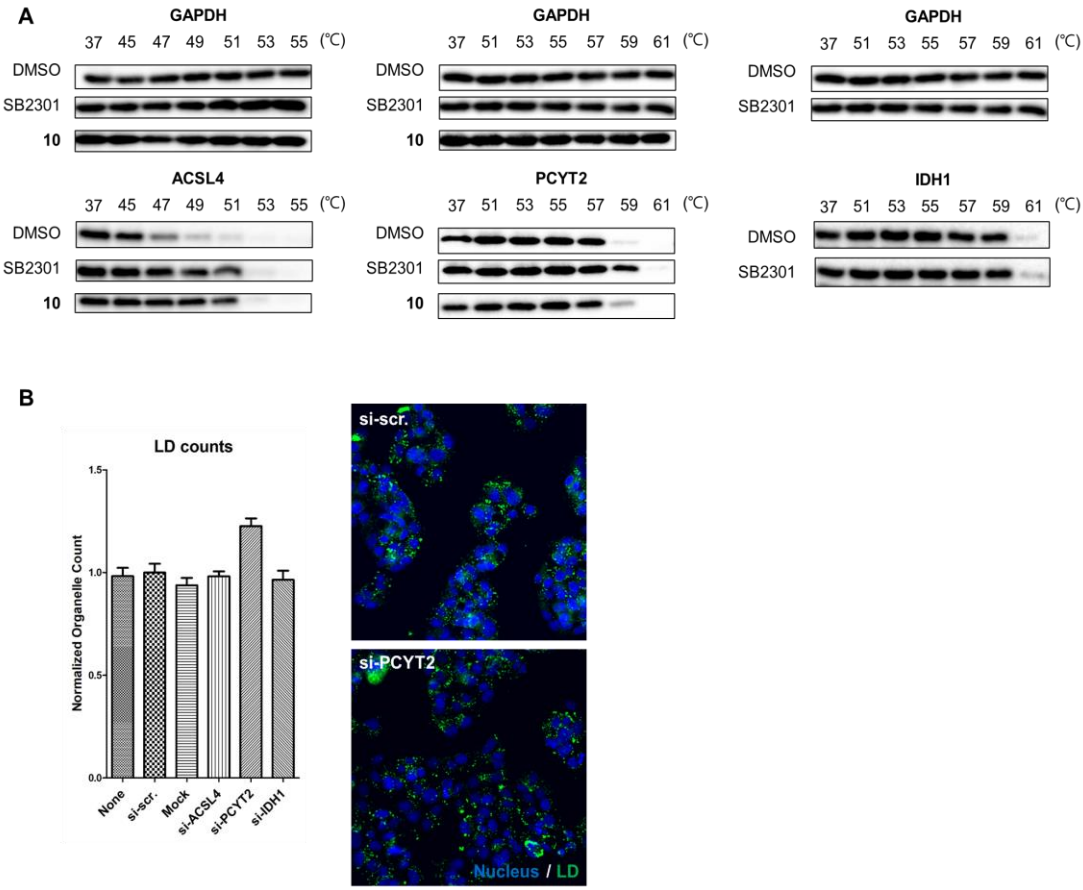

Figure 14. Target validation results. (A) 20 μM of **SB2301** and negative compound (**10**) were treated on HepG2 cells for 1 h. IDH1 did not show thermal stability shift on CETSA. **(B)** Loss of function study result. si-RNAs for each protein were treated on HepG2 cells for 48 h. After 48 h, LD fluorescence images were obtained.

Then, surface plasmon resonance (SPR) was conducted to determine the direct binding between **SB2301** and PCYT2. **SB2301** bound to PCYT2 in 1:1 binding mode, but a negative compound (**10**) did not (**Fig. 15A, 15B**). The calculated equilibrium dissociation constant (K_D) value between PCYT2 and **SB2301** was 26 μM, which is higher than IC_{50} value of **SB2301**. However, the interaction between PCYT2 and **SB2301** derivatives showed the same pattern with LD reduction activity. For instance, the compound that lack LD reduction activity (**10**) did not bind with PCYT2, and compounds with moderate LD reduction activity (**14**) showed direct binding with PCYT2 (**Fig. 15B, 15C**). Therefore, I concluded that PCYT2 could be a potential target protein of **SB2301**.

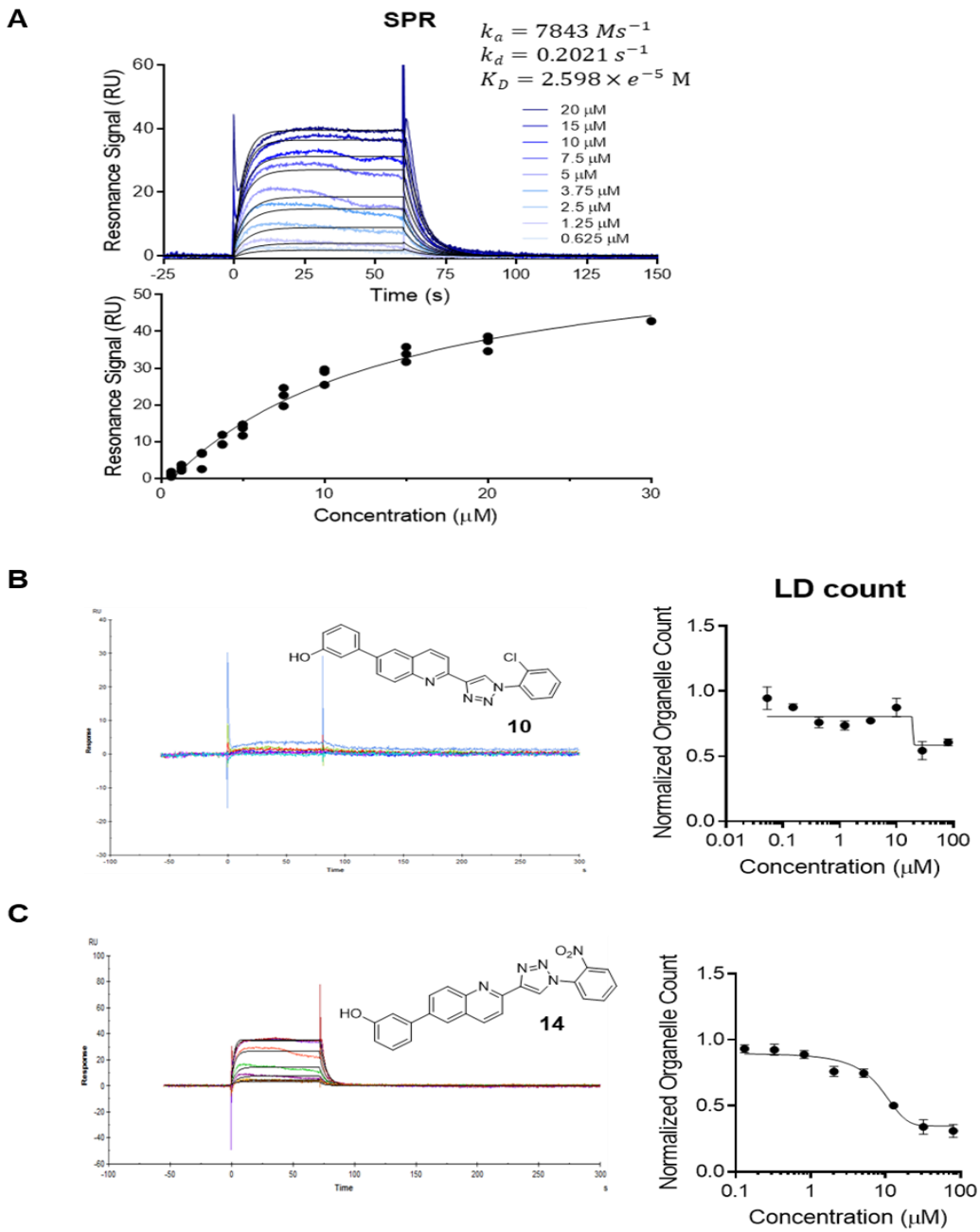

Figure 15. SPR results. Representative sensorgrams of surface plasmon resonance (SPR) analysis toward human PCYT2 (left) and dose-dependent LD-reducing activity (right) of **SB2301** derivatives. **(A) SB2301 (B) 10 (C) 14**.

3.6. The relationship between PCYT2 and LD coalescence.

I selected PCYT2 as a target protein of **SB2301**. Because PCYT2 showed direct binding with **SB2301**, also its function is highly related to determining LD morphology. PCYT2 is an enzyme that involves phosphatidylethanolamine (PE) biosynthesis.[35] Kennedy pathway is a well-known PE biosynthesis pathway, and PCYT2 catalyzes a rate-determining step of this pathway (**Fig. 16A**).[36] Many reports have reported that PE/PC ratio on LD membrane is a determinant of LD size.[37-40] For instance, when the phosphatidylcholine (PC) biosynthesis pathway is blocked by knockout *PCYT1* gene, an essential enzyme for PC synthesis, large LDs were formed.[38] This phenomenon is occurred due to the physical properties of phospholipids. The main phospholipid components of the LD membrane are PE and PC.[41] Since the polar head of PE is smaller than PC, PC occupies space in a cylindrical shape, whereas PE occupies space in a corn shape.[39] Due to these different biophysical properties between two phospholipids, the size of LD is determined as the entropically most stable state according to the given PE/PC ratio. Therefore, when the amount of PE increased, LDs lost their stability, then spontaneously merged to minimize the surface tension (**Fig. 16B**).

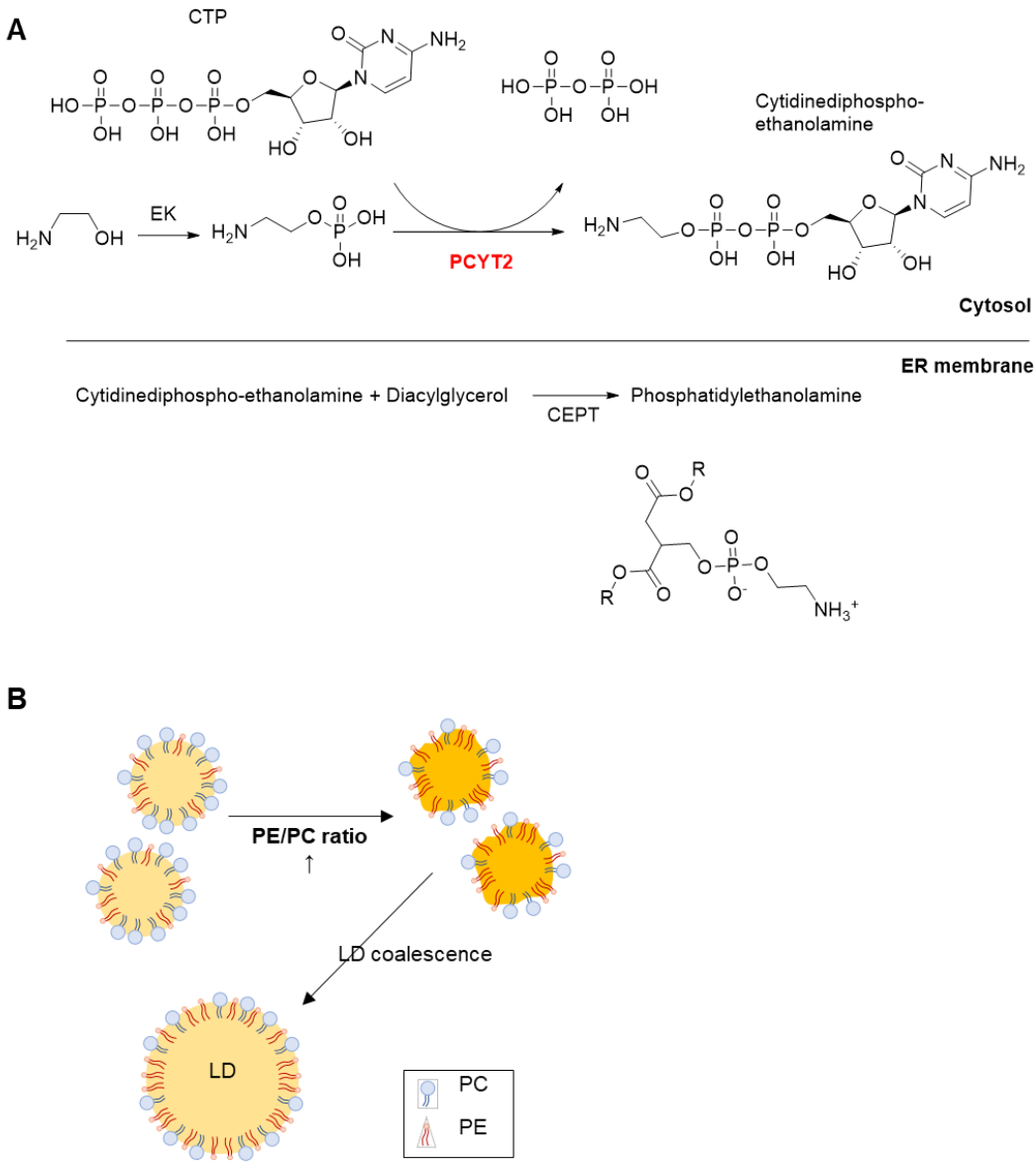

Figure 16. The relationship between PCYT2 and LD coalescence. (A) Schematic figure to show PE biosynthesis pathway (Kennedy pathway). **(B)** Schematic figure to establish the relationship between PE/PC ratio and LD coalescence.

According to the relationship between PCYT2 and LD coalescence, I inferred that **SB2301** increases PCYT2 activity. For LD coalescence, PE/PC ratio has to be increased on the LD membrane, which means PE biosynthesis is activated after **SB2301** treatment. To confirm this hypothesis, I isolated LDs from HepG2 cells and measured PE/PC ratio. Also, I conducted an enzymatic assay with purified PCYT2 to measure its activity upon **SB2301** treatment.

First, I isolated LDs from **SB2301** treated HepG2 cells to analyze the PE/PC ratio on the LD membrane. The LDs isolated from **SB2301** treated cells had a bigger size than DMSO treated condition (**Fig. 17A, 17B**). As expected, the PE/PC ratio on the LD membrane is increased after **SB2301** treatment (**Fig. 17C**). According to this data, I concluded that increment of PE/PC ratio on LD surface is a major factor to induce LD coalescence.

Next, I measured PCYT2 activity upon **SB2301** treatment (**Fig. 17D**). Unexpectedly, PCYT2 activity was not affected by **SB2301**. Also, the amount of PE in the entire cell was not affected either (**Fig. 17E**). These results imply that there is another mechanism for modulating PCYT2 activity and PE/PC ratios on the LD surface.

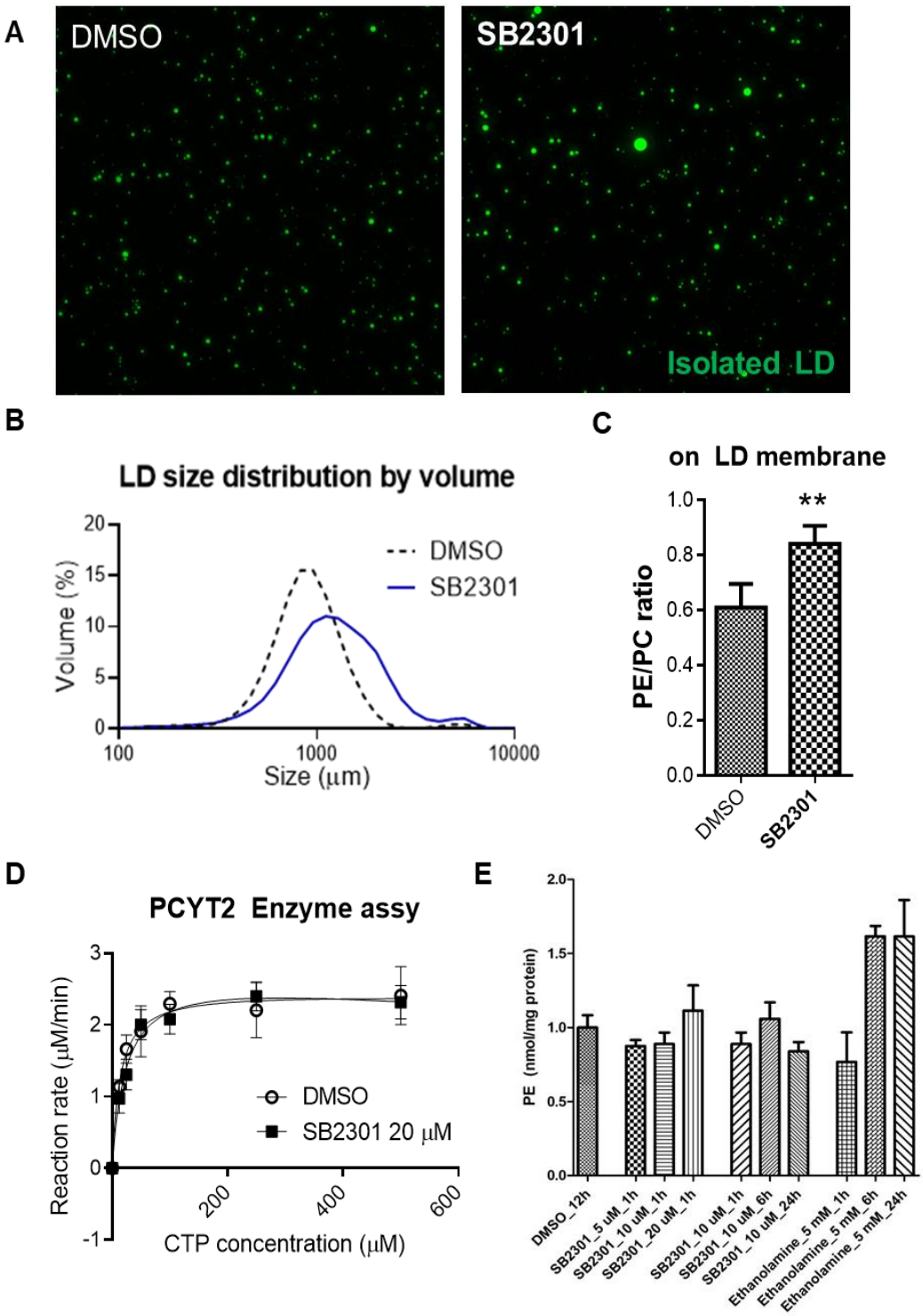
A
DMSO
SB2301
Isolated LD
B
LD size distribution by volume
Volume (%)
Size (μm)
DMSO
SB2301
C
on LD membrane
PE/PC ratio
**
DMSO
SB2301
D
PCYT2 Enzyme assy
Reaction rate (μM/min)
CTP concentration (μM)
DMSO
SB2301 20 μM
E
PE (nmol/mg protein)
DMSO_12h
SB2301_5 uM_1h
SB2301_10 uM_1h
SB2301_20 uM_1h
SB2301_10 uM_1h
SB2301_10 uM_6h
SB2301_10 uM_24h
Ethanolamine_5 mM_1h
Ethanolamine_5 mM_6h
Ethanolamine_5 mM_24h

Figure 17. SB2301 modulates the PE/PC ratio on the LD surface but not affects PCYT2 activity. (A) Representative isolated LD images of each condition. **(B)** The size distribution of isolated LDs. Dynamic light scattering (DLS) was used to measure size distribution. **(C)** The PE/PC ratio on the LD membrane. **(D)** PCTY2 enzymatic assay results. **(E)** The amount of PE in the entire cell.

To explain how **SB2301** increases the PE/PC ratio on the LD surface without affecting PCYT2 activity. I conducted immunofluorescence to visualize PCYT2 location. There was a previous report that PCYT1 moves to the LD surface when PC biosynthesis pathway is activated.[38] Similarly, I hypothesized that **SB2301** did not regulate the function of PCYT2, but it affected the spatial distribution of PCYT2. As shown in **Fig. 18**, PCYT2 translocated to the LD surface in a short treatment time (within 1 h), and more translocation was induced over time and dose-dependent manner. The relationship between LD coalescence and PCYT2 translocation is under investigation.

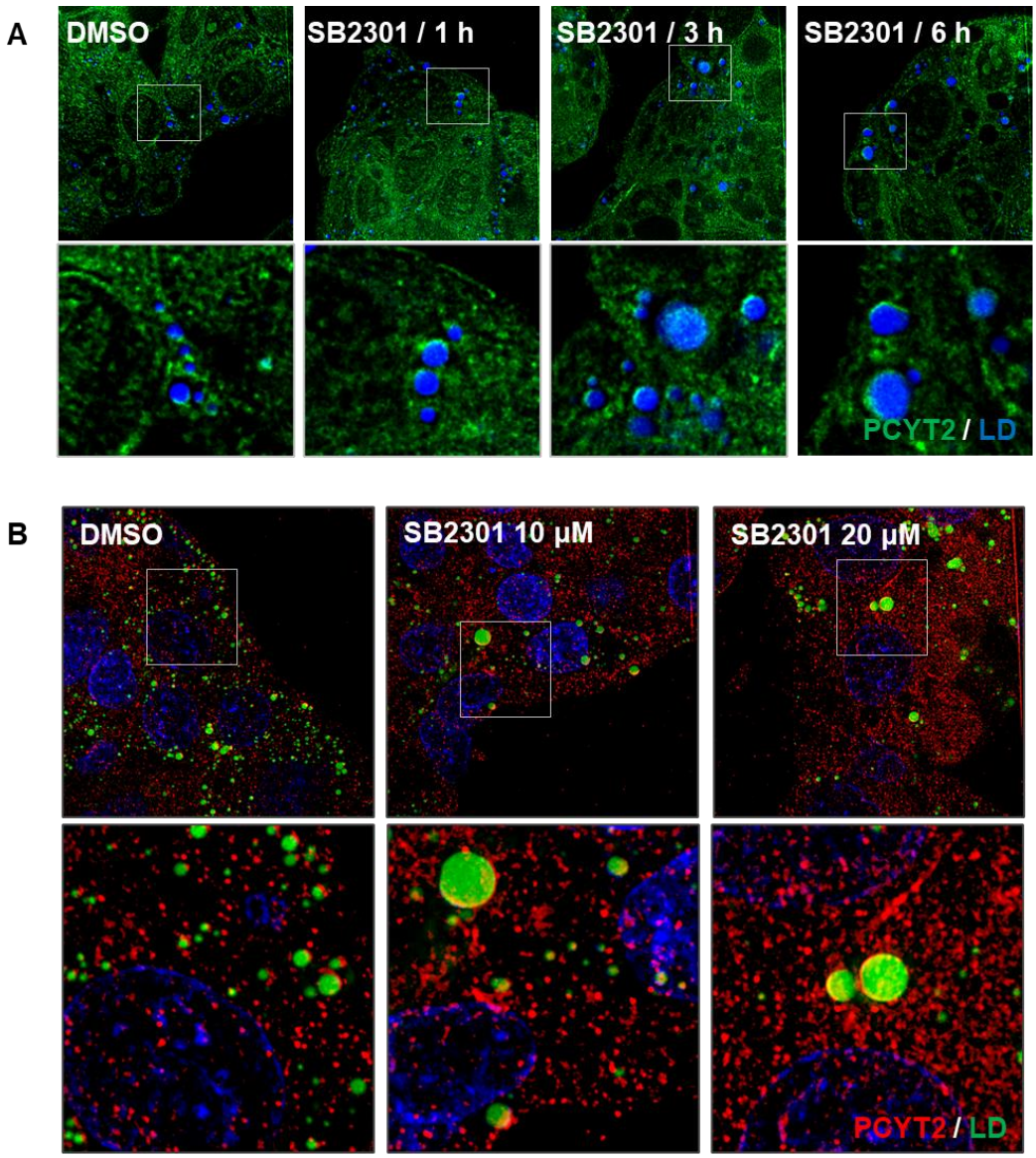

Figure 18. SB2301 affects the spatial distribution of PCYT2.

(A) Representative images of each condition. 20 μM of **SB2301** was treated on HepG2 cells at different times. **(B)** Representative images of each condition. **SB2301** was treated on HepG2 cells for 6 h.

4. Conclusion

Cellular LD plays an important role in energy homeostasis and lipid metabolisms by changing its forms over their environments, such as tissue types and energy conditions.[11] LD research field has emerged as a major interest in academic and industrial fields because of its importance in biological and physiological systems. Despite its importance, the regulatory mechanisms of cellular LDs are poorly elucidated, especially lipophagy.[20] Herein, I tried to approach this research field with a bioactive small molecule modulating LDs. I used an image-based high-throughput screening system to discover LD reducing small molecules. Because LD itself is regarded as a good phenotype representing cellular metabolic states. In addition, it is possible to approach an unbiased and varied manner, allowing to identify a novel LD modulation mechanism.

Through an image-based high-throughput screening system, I discovered **SB2301** which reduces cellular LDs without severe cytotoxicity. I then demonstrated that **SB2301** activates lipophagy by monitoring the sequestration of LDs into autophagosomes and autolysosomes, which leads to lysosomal degradation. Interestingly, **SB2301** treatment increased the ubiquitination of the LD proteome. Although ubiquitin-mediated lipophagy has not been reported, the cargo recognition for selective autophagy has known to be mediated by ubiquitin.[27-30] So, this observation strongly suggests that the

ubiquitin-mediated lipophagy mechanism exists. Broad proteomic studies are expected to clarify the remaining questions. For instance, which proteins on the LD surface are ubiquitinated and how ubiquitin-coated LDs are recognized and sequestered into autophagosomes. These studies will be allowing us to understand the process of ubiquitin-mediated lipophagy better.

Based on TS-FITGE and biophysical assays, PCYT2 was identified as a target protein of **SB2301**. **SB2301** controlled the spatial distribution of PCYT2 without affecting its enzymatic activity. I suppose that the **SB2301**-mediated translocation of PCYT2 causes the increment of the PE/PC ratio on the LD surface. Increased PE/PC ratio influences the biophysical stability of LDs and induces LD coalescence to minimize the surface tension. Currently, it is unclear how **SB2301** controls the spatial distribution of PCYT2. However, the results shown in this study will serve as a starting point to unveil the detailed molecular mechanism of the PCYT2 translocation and ubiquitin-mediated lipophagy.

The ubiquitin-mediated lipophagy mechanism investigated in this study reduces the intracellular fat content without inducing severe lipotoxicity. Because free fatty acids generated from degraded LDs were safely consumed in mitochondria. In addition, significant LD reduction in drug-induced *in vitro* steatosis model is verified. Thus, this newly discovered mechanism can be applied to drug discovery.

In conclusion, I discovered **SB2301** with a phenotype-based

approach to explore the unknown lipophagy mechanism. The newly discovered **SB2301** activated ubiquitin-mediated lipophagy and dynamically changed the size of the LDs. The LD membrane composition changed through PCYT2 translocation is a major factor to modulate LD morphology. I demonstrated that cells sensed the PE/PC ratio of the LD membrane and activated lipophagy to maintain homeostasis. Since this mechanism could safely and effectively reduce cellular LDs, it can be applied to a steatosis disease treatment strategy.

References

1 Olzmann, J. A. & Carvalho, P. Dynamics and functions of lipid droplets. *Nat Rev Mol Cell Biol* **20**, 137-155, doi:10.1038/s41580-018-0085-z (2019).

2 Farese, R. V., Jr. & Walther, T. C. Lipid droplets finally get a little R-E-S-P-E-C-T. *Cell* **139**, 855-860, doi:10.1016/j.cell.2009.11.005 (2009).

3 Benador, I. Y. *et al.* Mitochondria Bound to Lipid Droplets Have Unique Bioenergetics, Composition, and Dynamics that Support Lipid Droplet Expansion. *Cell Metab* **27**, 869-885 e866, doi:10.1016/j.cmet.2018.03.003 (2018).

4 Foster, D. W. Malonyl-CoA: the regulator of fatty acid synthesis and oxidation. *J Clin Invest* **122**, 1958-1959, doi:10.1172/jci63967 (2012).

5 Song, J. E. *et al.* Mitochondrial Fission Governed by Drp1 Regulates Exogenous Fatty Acid Usage and Storage in Hela Cells. *Metabolites* **11**, doi:10.3390/metabo11050322 (2021).

6 Molina, A. J. *et al.* Mitochondrial networking protects beta-cells from nutrient-induced apoptosis. *Diabetes* **58**, 2303-2315, doi:10.2337/db07-1781 (2009).

7 Shpilka, T. *et al.* Fatty acid synthase is preferentially degraded by autophagy upon nitrogen starvation in yeast. *Proc Natl Acad Sci U S A* **112**, 1434-1439, doi:10.1073/pnas.1409476112 (2015).

8 Toyama, E. Q. *et al.* Metabolism. AMP-activated protein kinase mediates mitochondrial fission in response to energy stress. *Science* **351**, 275-281, doi:10.1126/science.aab4138 (2016).

9 Liu, K. & Czaja, M. J. Regulation of lipid stores and metabolism by lipophagy. *Cell Death Differ* **20**, 3-11, doi:10.1038/cdd.2012.63 (2013).

10 Schott, M. B. *et al.* Lipid droplet size directs lipolysis and lipophagy catabolism in hepatocytes. *J Cell Biol* **218**, 3320-3335, doi:10.1083/jcb.201803153 (2019).

11 Zechner, R., Madeo, F. & Kratky, D. Cytosolic lipolysis and lipophagy: two sides of the same coin. *Nat Rev Mol Cell Biol* **18**, 671-684, doi:10.1038/nrm.2017.76 (2017).

12 Watt, M. J. & Steinberg, G. R. Regulation and function of triacylglycerol lipases in cellular metabolism. *Biochem J* **414**, 313-325, doi:10.1042/BJ20080305 (2008).

13 DiPilato, L. M. *et al.* The Role of PDE3B Phosphorylation in the Inhibition of Lipolysis by Insulin. *Mol Cell Biol* **35**, 2752-2760, doi:10.1128/MCB.00422-15 (2015).

14 Singh, R. *et al.* Autophagy regulates lipid metabolism. *Nature* **458**, 1131-1135, doi:10.1038/nature07976 (2009).

15 Schulze, R. J., Sathyanarayan, A. & Mashek, D. G. Breaking fat: The regulation and mechanisms of lipophagy. *Biochim Biophys Acta Mol Cell Biol Lipids* **1862**, 1178-1187, doi:10.1016/j.bbalip.2017.06.008 (2017).

16 Sathyanarayan, A., Mashek, M. T. & Mashek, D. G. ATGL Promotes Autophagy/Lipophagy via SIRT1 to Control Hepatic Lipid Droplet Catabolism. *Cell Rep* **19**, 1-9, doi:10.1016/j.celrep.2017.03.026 (2017).

17 Ward, C. *et al.* Autophagy, lipophagy and lysosomal lipid storage disorders. *Biochim Biophys Acta* **1861**, 269-284, doi:10.1016/j.bbalip.2016.01.006 (2016).

18 Nair, U., Thumm, M., Klionsky, D. J. & Krick, R. GFP-Atg8 protease protection as a tool to monitor autophagosome biogenesis. *Autophagy* **7**, 1546-1550, doi:10.4161/auto.7.12.18424 (2011).

19 Ni, H. M. *et al.* Dissecting the dynamic turnover of GFP-LC3 in the autolysosome. *Autophagy* **7**, 188-204, doi:10.4161/auto.7.2.14181 (2011).

20 Kounakis, K., Chaniotakis, M., Markaki, M. & Tavernarakis, N. Emerging Roles of Lipophagy in Health and Disease. *Front Cell Dev Biol* **7**, 185, doi:10.3389/fcell.2019.00185 (2019).

21 Grefhorst, A., van de Peppel, I. P., Larsen, L. E., Jonker, J. W. & Holleboom, A. G. The Role of Lipophagy in the Development and Treatment of Non-Alcoholic Fatty Liver Disease. *Front Endocrinol (Lausanne)* **11**, 601627, doi:10.3389/fendo.2020.601627 (2020).

22 Madeo, F., Carmona-Gutierrez, D., Hofer, S. J. & Kroemer, G. Caloric Restriction Mimetics against Age-Associated Disease: Targets, Mechanisms, and Therapeutic Potential. *Cell Metab* **29**, 592-610, doi:10.1016/j.cmet.2019.01.018 (2019).

23 Gatica, D., Lahiri, V. & Klionsky, D. J. Cargo recognition and degradation by selective autophagy. *Nat Cell Biol* **20**, 233-242, doi:10.1038/s41556-018-0037-z (2018).

24 Klionsky, D. J. *et al.* Guidelines for the use and interpretation of assays for monitoring autophagy (3rd edition). *Autophagy* **12**, 1-222, doi:10.1080/15548627.2015.1100356 (2016).

25 Ito, M. *et al.* Inhibition of Autophagy at Different Stages by ATG5 Knockdown and Chloroquine Supplementation Enhances Consistent Human Disc Cellular Apoptosis and Senescence Induction rather than Extracellular Matrix Catabolism. *Int J Mol Sci* **22**, doi:10.3390/ijms22083965 (2021).

26 Rogov, V., Dotsch, V., Johansen, T. & Kirkin, V. Interactions between autophagy receptors and ubiquitin-like proteins form the molecular basis for selective autophagy. *Mol Cell* **53**, 167-178, doi:10.1016/j.molcel.2013.12.014 (2014).

27 Kirkin, V., McEwan, D. G., Novak, I. & Dikic, I. A role for ubiquitin in selective autophagy. *Mol Cell* **34**, 259-269,

doi:10.1016/j.molcel.2009.04.026 (2009).
28 Kane, L. A. *et al.* PINK1 phosphorylates ubiquitin to activate Parkin E3 ubiquitin ligase activity. *J Cell Biol* **205**, 143-153, doi:10.1083/jcb.201402104 (2014).
29 Koyano, F. *et al.* Ubiquitin is phosphorylated by PINK1 to activate parkin. *Nature* **510**, 162-166, doi:10.1038/nature13392 (2014).
30 Thurston, T. L., Ryzhakov, G., Bloor, S., von Muhlinen, N. & Randow, F. The TBK1 adaptor and autophagy receptor NDP52 restricts the proliferation of ubiquitin-coated bacteria. *Nat Immunol* **10**, 1215-1221, doi:10.1038/ni.1800 (2009).
31 Lu, K., Psakhye, I. & Jentsch, S. Autophagic clearance of polyQ proteins mediated by ubiquitin-Atg8 adaptors of the conserved CUET protein family. *Cell* **158**, 549-563, doi:10.1016/j.cell.2014.05.048 (2014).
32 Schroeder, B. *et al.* The small GTPase Rab7 as a central regulator of hepatocellular lipophagy. *Hepatology* **61**, 1896-1907, doi:10.1002/hep.27667 (2015).
33 Divakaruni, A. S., Paradyse, A., Ferrick, D. A., Murphy, A. N. & Jastroch, M. Analysis and interpretation of microplate-based oxygen consumption and pH data. *Methods Enzymol* **547**, 309-354, doi:10.1016/B978-0-12-801415-8.00016-3 (2014).
34 Park, H., Ha, J., Koo, J. Y., Park, J. & Park, S. B. Label-free target identification using in-gel fluorescence difference via thermal stability shift. *Chem Sci* **8**, 1127-1133, doi:10.1039/c6sc03238a (2017).
35 Bakovic, M., Fullerton, M. D. & Michel, V. Metabolic and molecular aspects of ethanolamine phospholipid biosynthesis: the role of CTP:phosphoethanolamine cytidylyltransferase (Pcyt2). *Biochem Cell Biol* **85**, 283-300, doi:10.1139/o07-006 (2007).
36 Gohil, V. M. *et al.* Meclizine inhibits mitochondrial respiration through direct targeting of cytosolic phosphoethanolamine metabolism. *J Biol Chem* **288**, 35387-35395, doi:10.1074/jbc.M113.489237 (2013).
37 Fei, W. *et al.* A role for phosphatidic acid in the formation of "supersized" lipid droplets. *PLoS Genet* **7**, e1002201, doi:10.1371/journal.pgen.1002201 (2011).
38 Krahmer, N. *et al.* Phosphatidylcholine synthesis for lipid droplet expansion is mediated by localized activation of CTP:phosphocholine cytidylyltransferase. *Cell Metab* **14**, 504-515, doi:10.1016/j.cmet.2011.07.013 (2011).
39 Yang, H., Galea, A., Sytnyk, V. & Crossley, M. Controlling the size of lipid droplets: lipid and protein factors. *Curr Opin Cell Biol* **24**, 509-516, doi:10.1016/j.ceb.2012.05.012 (2012).
40 Arisawa, K., Ichi, I., Yasukawa, Y., Sone, Y. & Fujiwara, Y. Changes in the phospholipid fatty acid composition of the lipid droplet during

the differentiation of 3T3-L1 adipocytes. *J Biochem* **154**, 281-289, doi:10.1093/jb/mvt051 (2013).
41 Fei, W. *et al.* The size and phospholipid composition of lipid droplets can influence their proteome. *Biochem Biophys Res Commun* **415**, 455-462, doi:10.1016/j.bbrc.2011.10.091 (2011).

국 문 초 록

자가포식작용을 유도하는 물질을 통한 새로운 지방방울 제거 메커니즘의 발굴

박종범

서울대학교 대학원

화학부 화학생물학 전공

세포가 지방방울에 저장되어 있는 지방을 에너지원으로 사용하는 방법은 2가지가 있다. Lipolysis와 lipophagy이다. Lipophagy는 선택적인 자가포식작용의 한 예시로 2009년에 처음 보고된 이후, 지방 대사에서 중요한 역할을 담당한다는 사실이 꾸준히 보고되고 있다. 예를 들면 lipophagy에 문제가 생기는 경우에 비알코올성 지방간과 같은 다양한 대사질환이 발병된다는 연구결과가 있다. 이러한 중요성에도 불구하고, lipophagy는 다른 종류의 자가포식작용에 비해 구체적인 조절 메커니즘이 밝혀지지 않았다. 뿐만 아니라 lipophagy를 유도하는 적절한 물질이 없다는 것도 lipophagy 연구에 큰 걸림돌이 되고 있다.

본 학위 논문은 lipophagy를 유도하는 물질인 SB2301에 대해서 보

고하고자 한다. SB2301은 lipophagy를 유도할 수 있는 물질로, 이미지 기반 스크리닝을 통해 pDOS 라이브러리로부터 발굴되었다. 작용기전 연구를 통해 SB2301이 지방방울 표면의 인지질 조성을 바꾼다는 것이 밝혀졌으며, 이는 지방방울을 불안정하게 만드는 원인이 된다. 불안정한 지방방울은 자발적으로 합쳐지며 커다란 지방방울을 형성하고, 최종적으로 유비퀴틴화 되어 제거된다. SB2301이 자가포식작용을 유도하는 과정을 연구하면서 ubiquitin-mediated lipophagy라는 메커니즘의 존재를 처음 밝혔으며, 지방방울 표면의 인지질 조성을 바꾸는 것 만으로도 lipophagy를 활성화시킬 수 있다는 것이 밝혀졌다. 본 연구는 lipophagy를 연구하는데 있어서 하나의 이정표가 될 것이다.

주요어 : 지방방울의 자가포식작용, 생리활성 저분자 물질, 인지질 조성, 유비퀴틴 매게 자가포식작용

학 번 : 2019-26485